

Polarization Vortices in a Ferromagnetic Metal via Twistronics

Yingzhuo Lun^{1,2,#,*}, Xinxin Hu^{2,3,#}, Qi Ren^{1,#}, Umair Saeed^{2,3}, Kapil Gupta², Bernat Mundet², Ivan Pinto-Huguet^{2,3}, José Santiso², Jessica Padilla-Pantoja², José Manuel Caicedo Roque², Yunpeng Ma⁴, Qian Li⁴, Gang Tang¹, David Pesquera², Xueyun Wang¹, Jiawang Hong^{1,5,*}, Jordi Arbiol^{2,6,*}, and Gustau Catalan^{2,6,*}

¹School of Aerospace Engineering, Beijing Institute of Technology, Beijing 10081, China

²Catalan Institute of Nanoscience and Nanotechnology - ICN2 (CSIC & BIST), Barcelona, Catalonia 08193, Spain

³Autonomous University of Barcelona, Barcelona, Catalonia 08193, Spain

⁴State Key Laboratory of New Ceramic Materials, School of Materials Science and Engineering, Tsinghua University, Beijing 10084, China

⁵Beijing Institute of Technology (Zhuhai), Zhuhai 519088, China

⁶Institució Catalana de Recerca i Estudis Avançats (ICREA), Barcelona 08010, Catalonia

#These authors contributed equally to this work.

*Corresponding author emails: lunyingzhuo@bit.edu.cn (Y.L.), hongjw@bit.edu.cn (J.H.), arbiol@icrea.cat (J.A.), gustau.catalan@icn2.cat (G.C.)

Abstract

Recent advances in moiré engineering provide new pathways for manipulating lattice distortions and electronic properties in low-dimensional materials. Here, we demonstrate that twisted stacking can induce dipolar vortices in metallic SrRuO₃ membranes, despite the presence of free charges that would normally screen depolarizing fields and dipole-dipole interactions. These polarization vortices are correlated with moiré-periodic flexoelectricity induced by shear strain gradients, and exhibit a pronounced dependence on the twist angle. In addition, multiferroic behavior emerges below the ferromagnetic Curie temperature of the films, whereby polarization and ferromagnetism coexist and compete, showing opposite twist-angle dependencies of their respective magnitudes. Density functional theory calculations provide insights into the microscopic origin of these observations. Our findings extend the scope of polarization topology design beyond dielectric materials and into metals.

Since the discovery of superconductivity in twisted bilayer graphene¹, the field of so-called “twistronics”^{2,3} has blossomed. The key idea behind twistronics is that stacking two thin crystalline layers rotated with respect to each other generates a moiré interference pattern in the electronic density of states at the interface, which in turn modifies the electronic properties of the bilayer system. Twistronics was initially studied in the context of two-dimensional (2D) materials⁴, which can be readily exfoliated and stacked. The development of methods for growing epitaxial films of complex oxides and separating them from the substrate *via* dissolution of a sacrificial layer⁵⁻⁷ allows these materials to partake in the twistronic game. A seminal result in this context has been the discovery that two layers of BaTiO₃ twisted with respect to each other display polarization vortices⁸. The proposed explanation is that the torsional strain introduced at the interface between the twisted layers is not homogeneous, being minimal at the sites where the atomic columns of the two layers coincide across the interface, and maximal where equivalent atomic columns of the two layers are furthest apart. This causes torsional strain gradients and therefore gradient-induced polarization, known as flexoelectricity^{9,10}.

Flexoelectricity is allowed in materials of any symmetry¹¹, and twist-induced polar vortices have also been reported in SrTiO₃¹², which is cubic and non-polar in the absence of strain (although strain can make it ferroelectric¹³). Since there are not strain gradients without strain, it can be difficult to separate how much of the polarization vortices is due to gradient-induced flexoelectricity, and how much to strain-induced ferroelectricity or piezoelectricity. While piezoelectricity has been ruled out from the explanation of vortices based on geometrical considerations, the fact remains that there is a strong polarization to start with that may be affected both by strain and by the depolarization fields expected whenever polarization is disrupted. It is therefore highly desirable to examine whether polar vortices can be induced in a material where piezoelectricity and/or depolarization fields can be fully excluded. Importantly, if the origin of polar vortices is truly flexoelectric, we no longer need to limit ourselves to examining insulating materials in our on-going search for chiral polarization^{14,15}: metals can also be flexoelectric¹⁶⁻¹⁸. Therefore, a tantalizing possibility emerges of inducing polarization vortices in a metal, where the depolarization field engineering approach typically used in ferroelectrics is just not available.

In this work, we have fabricated twisted-bilayer (t-BL) stacks of SrRuO₃ (SRO), a well-known oxide metal whose flexoelectricity has been recently reported¹⁷, and we have combined atomic-scale imaging with theoretical calculations to examine the polar displacement pattern. The results show that the Ru cation is shifted with respect to the Sr lattice, forming periodic arrays of vortices and antivortices like those reported in insulating BaTiO₃ and SrTiO₃^{8,12}, displaying a significant twist-dependence. Moreover, we observed that the twisted-stacking induced polarization has functional consequences on the ferromagnetic and metallic properties, indicating multiferroic characteristics in metallic membranes.

Film growth and structural characterization

Epitaxial thin films of SRO (10.7 nm) were grown by pulsed-laser deposition (PLD) on (001)-oriented SrTiO₃ (STO) substrates with water-soluble Sr₃Al₂O₆ (SAO) buffer layer. The films were attached onto a polydimethylsiloxane (PDMS) stamp and immersed in deionized water to dissolve the SAO layer. Upon removal of SAO and separation of SRO from the substrates, the freestanding single-layer (SL) SRO membranes were transferred onto silicon oxide or TEM supports. The t-BL SRO was assembled by stacking a second membrane, released from the same epitaxial film and transferred onto the first one with a prescribed rotational angle. To remove potential surface adsorbates at the interface and/or hydrogen intercalation¹⁹, the transferred samples were annealed at 330 °C for 8 hours in an oxygen atmosphere before measurements. The schematic of fabrication process is provided in Fig. 1a, and further details for film growth and transfer are described in Methods.

The crystallinity of the initial epitaxial films and subsequently transferred membranes was confirmed by X-ray diffraction (XRD) 2 θ - ω scans (Fig. 1b). The fully epitaxial strained state of the as-grown heterostructures was confirmed using reciprocal space mapping (Fig. 1c), revealing that the SRO and SAO layers share the same in-plane lattice parameter as the STO substrate. The diffraction peak of the transferred membrane (Fig. 1b), however, is shifted, suggesting a relaxation of the lattice upon epitaxial strain release. The morphologies of the as-grown film and the transferred bilayer membrane (Fig. 1d and Supplementary Fig. S1) show smooth and flat surfaces with roughness of 0.25 nm and 0.38 nm, respectively. The bilayer interface was examined using cross-sectional scanning transmission electron microscopy with high-angle annular dark-field (STEM-HAADF) imaging (Supplementary Fig. S2). A high-quality interface with minimal interlayer distance of 4.97 Å is observed in the twisted bilayer.

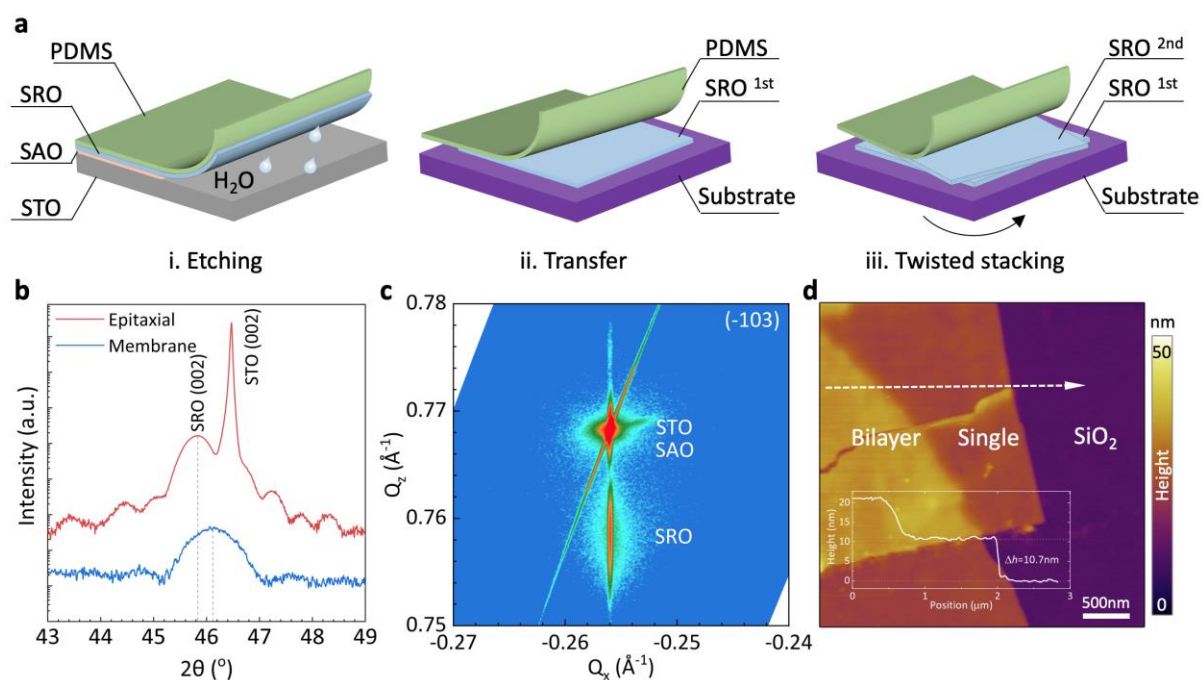


Figure 1. Transfer and characterization of twisted-bilayer SrRuO₃ membranes. **a**, Schematic illustration of the transfer process of twisted bilayer membranes. **b**, X-ray

diffraction 2θ - ω scans of the as-grown epitaxial film and transferred membrane (a.u., arbitrary units). **c**, Reciprocal space mapping of the as-grown film around the (-103) diffraction peak. **d**, Surface morphology of the transferred t-BL SRO membrane. The inset shows the line profile, indicating a thickness of 10.7 nm for a single layer.

Polarization vortices in twisted-bilayer SrRuO₃

We used high-resolution STEM-HAADF imaging to visualize the in-plane atomic structure of the metallic membranes and determine the eventual presence of polarization vortices (see Methods). Bulk SRO crystallizes in a centrosymmetric perovskite structure with orthorhombic symmetry (Pbnm) at room temperature²⁰. We found that, even when the size reduces to the nanometer scale, the freestanding SL SRO membrane retains its orthorhombic characteristics, as evidenced by the presence of $\frac{1}{2}$ superlattice spots in the selected area electron diffraction (SAED) pattern (Supplementary Fig. S3). To quantify polarization, we measured the off-center displacement of Ru (δ_{Ru}) with respect to its four adjacent Sr atoms. The Ru displacement extracted from the STEM-HAADF image of the SL SRO (Figs. 2a, e) is both random and minimal (1.3 pm on average), indicating that the freestanding SRO remains nonpolar as its bulk counterpart.

The t-BL SRO exhibits a different behaviour. Upon focusing the electron beam at the bilayer interface, a continuous and well-ordered moiré was found in low-magnification image (Supplementary Fig. S4), suggesting a homogeneous interfacial contact. Subsequent high-resolution moiré images measured from the 3.0°, 4.8°, and 7.3° twisted bilayers are shown in Figs. 2b-d, displaying a decreasing moiré periodicity with increasing twist angle. The twist angle was determined from the relative rotation between the two distinct sets of diffraction spots observed in the fast Fourier transform (FFT) of the moiré images (Supplementary Fig. S5). By shifting the focus away from the interface to the upper surface, we selectively imaged the lattice structure of the top layer (Supplementary Fig. S6). Prior to this, we conducted depth-dependent STEM imaging and analyzed the corresponding variations in FFT patterns. The results confirmed that the diffraction spots from the bottom lattice completely vanish as the focus shifts to the upper surface (Supplementary Fig. S7), thus excluding geometric interference artifacts from the bottom layer in the images obtained at top layer.

The Ru displacement maps of the top layers (Figs. 2f-h), calculated based on the lattice structure observed at STEM-HAADF images (Supplementary Fig. S6), reveal a periodic arrangement of alternating vortices and antivortices, indicating that chiral polarization has emerged in the metallic membranes. While chiral polarization is becoming increasingly frequent among ferroelectrics, where it can be driven either by depolarization field^{21,22} or torsional strain gradients⁸, it is unprecedented in SRO or any other metal. The toroidal moment was quantified as $\mathbf{Q}_i = \frac{1}{2N} \sum_1^N \mathbf{r}_i \times \delta_i$, where δ_i is the adjacent Ru displacement vector located at position \mathbf{r}_i , and $N = 24$ is the number of adjacent cells, and then superimposed onto the Ru displacement maps to visualize the spatial arrangement of polar vortices (Figs. 2f-h). The periodic array of negative toroidal moments reveals that the AA- stacked (Sr-Sr and Ru-Ru sites) regions host clockwise

vortices, while anticlockwise vortices form near the AB- stacked (Sr-Ru sites) regions. These features in polarization vortices can be robustly observed in the different bilayers even with a high twist angle of 10.4° (Supplementary Fig. S8) but were entirely absent in the SL SRO (Fig. 2e). As the twist angle increases, the periodicity of polar vortices in different bilayers becomes smaller, and always coincides with the moiré periodicity, consistent with the twistrionic origin of the polarization.

The magnitudes of the toroidal moment and the polarization also decrease as the twisting increases. Figure 2i shows that the Ru displacement exhibits an inverse dependence on the twist angle, being more significant at the smallest twist angle. The maximum displacement reaches ~ 20 pm (8.3 pm on average) for the 3.0° twisted bilayer, which is comparable to reported values for polarized SRO^{17,23,24}. To exclude the possibility that the observed polarization vortices arise from imaging artifacts associated with the moiré pattern, we performed the same measurements on unannealed samples. The idea is that a weaker interlayer coupling at the unannealed interface should make it difficult to distort the lattice and polarize it. Indeed, the unannealed samples remain non-polar, with a Ru displacement map (Supplementary Fig. S9) like that of SL SRO, despite the presence of a moiré pattern at the interface. The observed polarization vortices are therefore not a geometric interference artifact, since the moiré exists both in the annealed and unannealed bilayers.

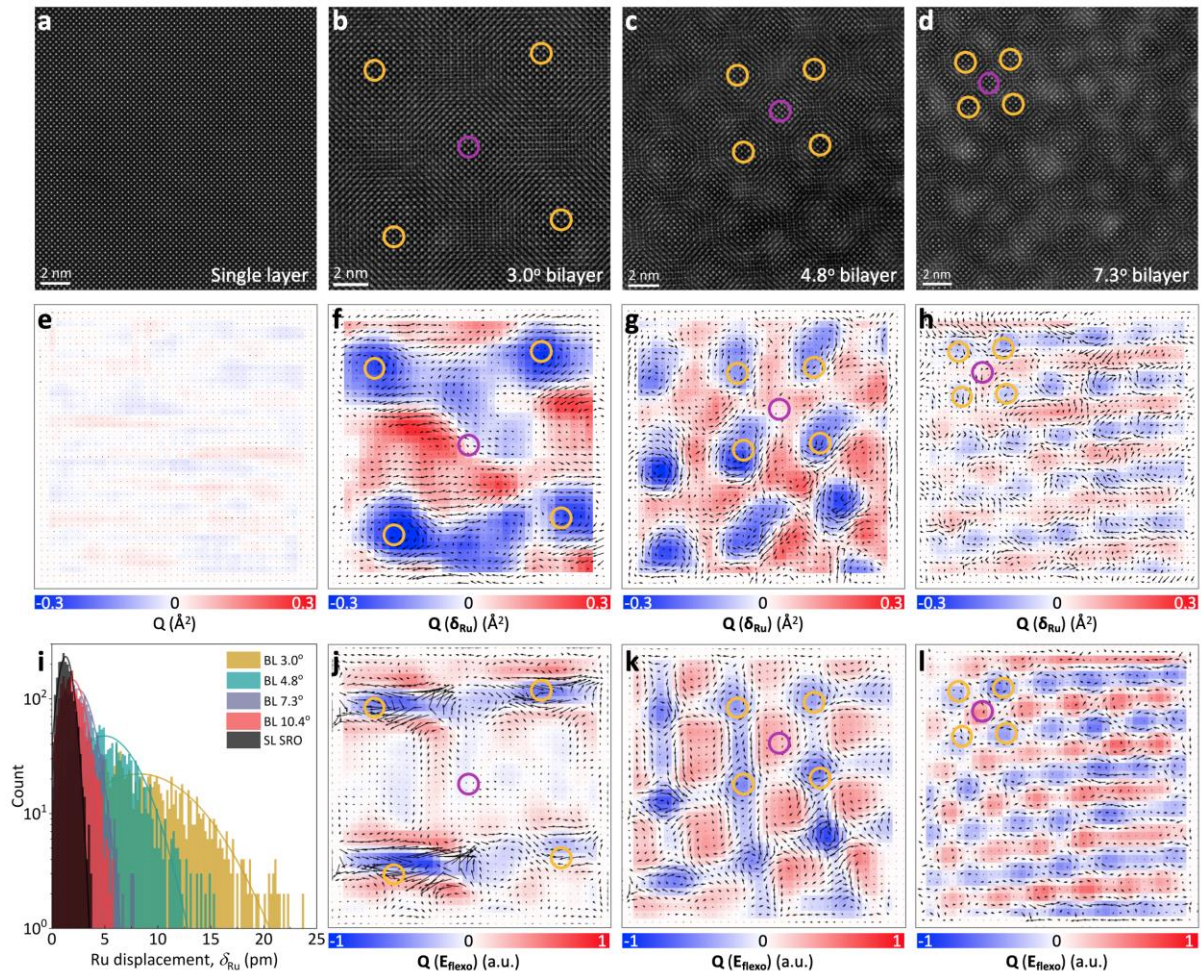


Figure 2. Atomic-scale imaging of polar vortices in t-BL SROs. **a**, Planar-view STEM-HAADF image of the freestanding SL SRO. **b-d**, Moiré images focusing on the interface in the 3.0°, 4.8°, 7.3° twisted bilayers, respectively. **e**, Ru displacement vector maps superimposed with their toroidal moment $Q(\delta_{\text{Ru}})$ for the SL SRO. **f-h**, Same Ru displacement analyses for the top layer in the 3.0°, 4.8°, 7.3° twisted bilayers, respectively. The Ru displacements in **e**, **f**, **g**, and **h** are amplified by factors of 30, 30, 50, 100 for clarity, respectively. **i**, Histograms comparing the magnitude of Ru displacement of SL and t-BL SROs. **j-l**, Normalized flexoelectric field vector maps reconstructed by shear strain gradients, superimposed with their toroidal moment $Q(E_{\text{flexo}})$. The yellow and purple circles in **b-d**, **f-h**, and **j-l** indicate the AA- and AB-stacked regions, respectively.

Since electrostatic interactions are expected to be screened by the free charges in metallic systems, whereas strain (gradient) cannot be screened, the polar vortices of the SRO bilayers consistent with a mechanical rather than electrostatic origin, lending support to the flexoelectric hypothesis^{8,25}: the periodic misalignment of the atoms in the top and bottom layers generates shear torsional strain gradients and thus flexoelectric fields, which can serve as pseudo-electric fields, manipulating polarization^{26,27} and driving the formation of polar vortices. The strain-gradient origin is further supported by the geometric phase analysis (GPA) (see Supplementary Text I), showing that the shear strain gradients are distributed in a strip network of alternating signs, with the polarization components pointing in the same direction within each strip region (Supplementary Fig. S10). A flexoelectric coupling in metals is evidenced as the polarization systematically switches towards the opposite direction upon the reversal of the strain gradients. The flexoelectric fields reconstructed by shear strain gradients (Figs. 3j-l) significantly correlate with the observed polar vortices maps, providing direct supports of a flexoelectric origin for the polar vortices. This electromechanical coupling accounts for the observed twist angle-dependent polarization, where the larger polarization at small angle is attributed to the more significant lattice distortion (shear strain) and its localized inhomogeneity (strain gradients).

DFT calculation for polarized t-BL SrRuO₃

We then used first-principles density functional theory (DFT) to simulate the polarization in t-BL SRO (see Methods). Commensurate bilayer supercell structure was constructed by stacking two individual unit-cell-thick layers with a relatively high twist angle of 18.92°. The smaller moiré periodicity with fewer atoms in a high-angle model improves computational efficiency. The established twisted bilayer model, depicted in Fig. 3a, exhibits a characteristic moiré pattern arising from alternating AA- and AB-stacked sequences. After fully relaxing structure, we computed the off-center displacement of Ru atoms relative to the surrounding oxygen octahedra in each unit cell. The corresponding maps (Figs. 3b-c) reveal the formation of polarization vortices in the top and bottom layers, with opposite chirality in each layer. In the top layer, clockwise vortices predominantly form at AA-stacked regions and rough anticlockwise ones at AB-stacked regions, consistent with our experimental observations. Similar polarization configuration can be robustly reproduced in bilayers with higher twist angles of 22.62°

and 28.07° (Supplementary Fig. S13). The calculated Ru displacement decreases with twist angle (Fig. 3d), in agreement with experimental results. Since the calculations adopted unit-cell-thick SRO layers, the lattice near the bilayer interface is expected to be subjected to larger strain, the magnitude of calculated polarization is thereby larger than the experimental one that measured at the upper surface. To demonstrate the crucial role of twisted stacking, we conducted the same calculations for 0° -stacked bilayers with different translational shifts; irrespective of AA- or AB-stacked bilayers, SRO maintains a centrosymmetric structure without any polarization (Supplementary Fig. S14). Additionally, we calculated the electronic density of states (DOS) of the polarized twisted bilayers (Fig. 3e and Supplementary Fig. S15). All twisted bilayers exhibit nonzero density of states at the Fermi level, primarily contributed by Ru *d*-orbital electrons, confirming their metallic nature. The overlap of the Ru *d* and O *p* states indicates a strong Ru-O orbital hybridization. Overall, our calculations provide solid theoretical evidence that topological polarization can be physically compatible with metallicity in twisted bilayers.

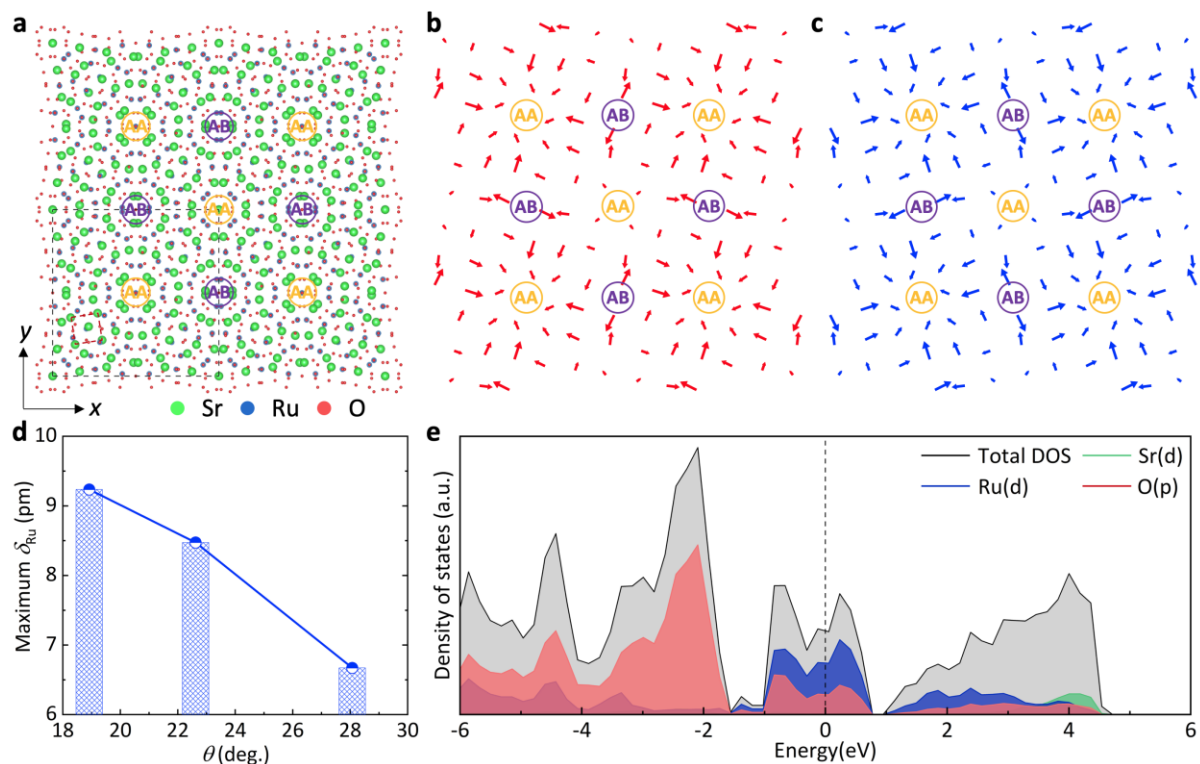


Figure 3. DFT calculation for polar vortices in metallic SRO. **a**, Planar view of constructed 2×2 supercell for the 18.92° twisted bilayer. The black and red dashed squares denote the supercell and unit cell of SRO, respectively. **b-c**, In-plane Ru displacement maps of the top (red) and bottom (blue) layers, respectively. All displacements are amplified by a factor of 25 for clarity. The AA- and AB-stacked regions are marked with yellow and purple circles, respectively. **d**, Maximum in-plane Ru displacements as functions of the twist angle, extracted from the calculations. **e**, Electronic density of states of the polarized twisted bilayer. The Fermi level is indicated by a dashed line.

Functional consequences of polar vortices

Having established the presence of polarization vortices in t-BL SROs, the question arises: do these vortices have any tangible impact on the material's functional properties? A consideration is that bulk SRO is a paramagnetic metal at room temperature, but it undergoes a transition to a ferromagnetic state below ~ 160 K²⁸ (~ 150 K for epitaxial films²⁹). This ferromagnetic ordering manifests as a distinct change in the electrical resistance^{30,31}. Given that polarization, conductivity, and magnetism are all closely linked to the Ru atoms and their surrounding oxygen octahedra, coupling among these properties may be possible.

With this in mind, we measured the temperature-dependent magnetization (M - T) curve and ferromagnetic hysteresis loop (M - H) for SL and t-BL SROs (see Methods). Figures 4a-b show that the t-BL SROs exhibit ferromagnetism with higher coercive field at low temperature. We examined the variation in ferromagnetic transition temperature and magnetic moment, which show strong dependencies on the twist angle. The Curie temperature T_C (inset of Fig. 4a) and the saturation magnetization M_s (hysteresis loops in Fig. 4b) both decrease as the twist angle is reduced. The twist-dependent T_C and M_s are summarized and compared with δ_{Ru} in Fig. 4c, showing that the polarization magnitude and the ferromagnetism display opposite trends with respect to the twist angle, suggesting a competition between the two types of ordering. We also measured the temperature-dependent resistance curves (Supplementary Fig. S16), which show that all samples exhibit typical metallic conductivity. The kink in resistance due to the ferromagnetic transition, highlighted in Fig. 4d, show the same twist angle-dependence. These results reveal coexistence and interaction of polar vortices and ferromagnetic ordering in correlated metallic systems, indicating that SRO becomes a “multiferroic metal” under the twisted stacking.

The apparent competition between polar and magnetic orderings echoes the known difficulty of stabilizing ferroelectricity and ferromagnetism within the same material^{32,33}. To understand this multiferroic competition, we constructed an orthorhombic SRO structure and modulated polarization by manually off-centering Ru cations, thus approximating the polarization observed in t-BL SROs. The magnetic exchange parameter of the Heisenberg model was calculated based on DFT total energies of ferromagnetic and anti-ferromagnetic phases (see Methods). The results shown in Fig. 4e indeed reveal a gradual decrease in the exchange parameter with increasing polarization, consistent with the observed lower magnetization. The reduced exchange interaction is attributed to the decreasing of the mean Ru-O-Ru bond angle due to the Ru displacement along the polar direction. This off-centering reduces the overlap between Ru 4d and O 2p orbitals, thereby weakening the Ru-O hybridization. The Curie temperature estimated based on exchange parameter also decreases with increasing polarization, in good agreement with the experimental observations (Fig. 4f).

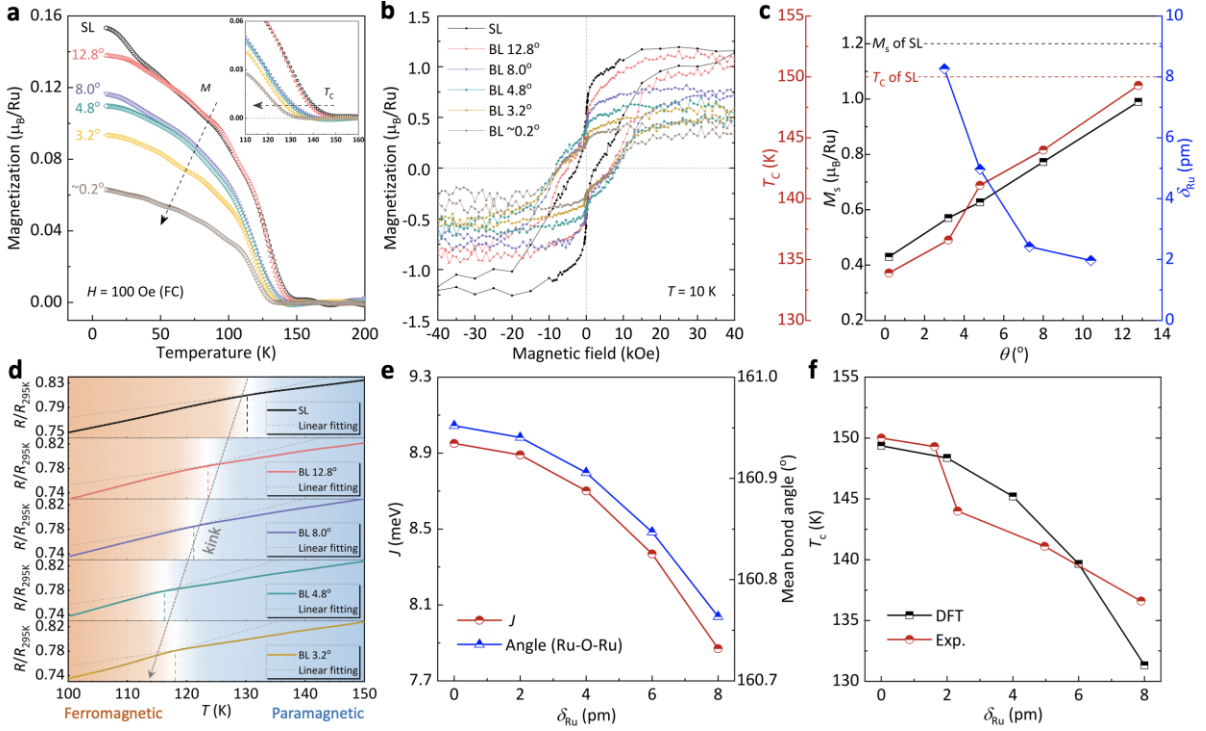


Figure 4. Magnetic and electrical transport characterizations of polarized t-BL SrRuO₃. **a**, Temperature-dependent magnetization field-cooling curves of SL and BL SROs measured under an in-plane magnetic field of 100 Oe. The inset highlights the variations in ferromagnetic transition temperature. **b**, In-plane ferromagnetic loops measured at 10 K. **c**, Twist-angle dependencies of ferromagnetic transition temperature (T_C), saturation magnetization (M_s) and Ru displacement (δ_{Ru}). The dashed lines indicate the T_C and M_s of SL SRO. The mean values of δ_{Ru} are extracted from the Gaussian fitting in Fig. 2i. **d**, Normalized temperature-dependent resistance curves. The vertical dashed lines indicate the kinks in resistance, which is determined by linearly fitting the local raw data on the right and left sides. **e**, Magnetic exchange parameter (J) and mean Ru-O-Ru bond angle as a function of Ru displacement. **f**, Comparison of T_C from DFT calculations and experiments. The experimental values were obtained via linear interpolation based on the mean $\bar{\delta}_{Ru}$ and T_C across samples with varying twist angles.

Conclusion

The discovery of polarization vortices in metallic membranes expands the field of polar topology^{34,35} into metals and strongly correlated electron systems^{36,37}. Our findings demonstrate that moiré engineering can induce polarization vortices in a metallic system, and, since SRO is also ferromagnetic, the result is a multiferroic metal. The results indicate an anticorrelation and therefore a possible competition between the two orders. Beyond SRO, our results highlight the broader implications of flexoelectricity as a universal property, suggesting that similar polarization phenomena could emerge in other twisted bilayer metallic systems. The presence of polarization within a metal introduces new degrees of freedom for spintronic applications, mediated by flexo-Rashba effect¹⁸, opening new avenues for designing materials with tunable electronic,

magnetic, and topological properties, and exploring potential polarization-related behaviour in metallic systems.

Methods

Epitaxial film growth

All epitaxial films were synthesized using pulsed-laser deposition (PLD) with a KrF excimer laser (248 nm, COMPex 102, Lambda Physik). The SrRuO₃ (SRO) thin films were grown on (100)-oriented SrTiO₃ (STO) substrates with an 8.8 nm-thick Sr₃Al₂O₆ (SAO) sacrificial layer to enable the subsequent membrane release. Prior to deposition, the chamber was evacuated to a base pressure of 1.0×10^{-4} mTorr. Stoichiometric ceramic targets were used to ensure the chemical composition of films. The SAO layer was deposited at 750 °C under an oxygen pressure of 1 mTorr, with a laser fluence of 1.60 J/cm². The SRO layer was subsequently grown at 700 °C under an oxygen pressure of 100 mTorr O₂, with a laser fluence of 1.28 J/cm². The laser repetition rate was maintained at 1 Hz throughout the deposition process. After deposition, the films were cooled down to room temperature at 5 °C/min under an oxygen pressure of 10 Torr.

Twisted bilayer membrane transfer

To obtain freestanding SRO membranes, the epitaxial films were adhered to a polydimethylsiloxane (PDMS) stamp and immersed in deionized water to dissolve the SAO sacrificial layer. The complete dissolution of SAO led to the detachment of the film from the substrate. The released membrane, attached to the PDMS stamp, was then transferred onto a target substrate using a transfer platform that allows to control the rotation of the substrate with a precision of 0.1°. Half of the membrane on the PDMS was brought into contact with the substrate, and the temperature was then increased to 40 °C to remove residual water. The PDMS was subsequently peeled off slowly, ensuring an intact transfer of the membrane. To make a twisted-bilayer sample, the substrate with the transferred bottom layer was rotated to a predefined angle using a micrometer probe in the transfer system. The remaining half of the membrane on the PDMS was then transferred onto the bottom one in the same manner, thereby obtaining twisted-bilayer samples. To enhance interlayer interaction and eliminate possible adsorbates at the interface, the samples were annealed at 330 °C for 8 hours under oxygen flow rate of 50 sccm.

X-ray diffraction (XRD) and surface characterizations

High-resolution 2θ - ω scans and reciprocal space mappings (RSMs) were conducted using a Panalytical X'pert Pro diffractometer with a Cu K α_1 (1.540598Å) source. The system featured a hybrid two-bounce primary monochromator on the incident beam side and a PIXcel line detector for high-resolution data acquisition. The surface morphology was characterized using MFP-3D Asylum AFM (Asylum Research -Oxford Instruments). Tapping mode was performed to minimize surface damage using a soft tip.

TEM, SAED, and STEM characterizations

The low-magnification HRTEM images and SAED patterns were acquired using a FEI Tecnai F20 TEM at 200 kV. High-quality cross-sectional samples were fabricated using the focused ion beam (FIB) technique at a Thermo Fisher Helios 5 UX dual-beam system. The STEM experiments were conducted using a double aberration-corrected Spectra 300 operated at 300 kV. Depth-sectioning STEM-HAADF was performed by acquiring a series of atomic-resolution images at different defocus depth⁸, allowing for discrimination between the top layer and the bilayer interface. STEM-HAADF images were acquired with a probe convergence semi-angle of 27.3 mrad while the HAADF detector collection semiangle was set as 63–200 mrad.

Polarization vortices and strain analysis

The atomic positions of Ru and Sr were firstly extracted from Wiener-filtered STEM-HAADF images using the Python package Atomap³⁸. After locating the Ru and Sr columns, the off-center displacement of each unit cell was calculated as the deviation of the Ru column from the mass center of the four adjacent Sr columns. The mean Ru displacement value is subtracted in the mappings to improve the visibility of the polarization vortex array. Strain analysis was performed using the Geometrical Phase Analysis (GPA)³⁹ software package (HREM Research) in Digital Micrograph.

Electrical transport and magnetization measurements

Temperature-dependent resistance measurements were performed in an Advanced Research Systems cryostat using a Keithley 2614B SourceMeter. The SL and t-BL membranes were transferred onto an insulating oxidized silicon substrate, and the Pt electrode arrays were sputtered through a square array-mask placed on the sample surface, defining 100 μm electrodes separated by 20 μm spacing. The electrodes were contacted via wire-bonding to a leadless chip carrier (Kyocera) electrically connected to the sourcemeter by a chip-carrier socket, and thermally connected to the cold finger of the cryostat. The resistance was measured using two-point contact mode, as the temperature gradually varied at a rate of 1 K/min. Ferromagnetic hysteresis loops and temperature-dependent magnetization field-cooling curves were measured using a vibrating sample magnetometer (VSM, Quantum Design MPMS-3). The SL and t-BL membranes were transferred onto sapphire substrates. The external magnetic field was applied parallel to the membrane plane.

DFT calculation for polar vortex

DFT calculations were performed using the Vienna Ab Initio Simulation Package (VASP)^{40,41}. The projector-augmented wave (PAW) method⁴² was employed, with the Perdew–Burke–Ernzerhof (PBE)⁴³ generalized gradient approximation (GGA)⁴⁴ used as the exchange-correlation functional. The cubic structure was adopted to construct bilayer supercell structures, following the method proposed by Lee et al.⁴⁵. The electronic wave functions were expanded using a plane-wave basis set with a kinetic energy cutoff of 600 eV and the 12 \times 12 \times 1 k-point mesh was used to sample the Brillouin zone. The monolayer structure was built based on the relaxed bulk SRO and was fully relaxed. The equilibrium lattice constant of cubic monolayer was calculated to be 3.781 Å, and the same value

was used for all bilayer structures. The $12 \times 12 \times 1$ k-mesh was used for monolayer and untwisted bilayer structures, whereas Γ -point sampling was adopted for the twisted structures. Structural relaxations were performed until the Hellmann-Feynman forces on each atom were reduced below 0.01 eV/\AA . Van der Waals interactions between adjacent layers were accounted for using the Grimme D3 method⁴⁶. To prevent spurious interlayer interactions, a vacuum region exceeding 15 \AA was introduced in the supercell.

DFT calculation for magnetism

The magnetic properties were investigated based on an orthorhombic structure with manually off-centering Ru along the c -axis direction (*i.e.* [001]-orientation), which lies within the membrane plane in as-grown film. In DFT calculations, a plane-wave basis set with a kinetic energy cutoff of 500 eV was used to expand the electronic wave functions, and an $8 \times 8 \times 6$ k-mesh was employed to sample the Brillouin zone. The on-site Coulomb interaction parameters were set to $U = 3 \text{ eV}$ and $J = 0.3 \text{ eV}$ for Ru 4d orbitals. The Curie temperature was estimated using the Heisenberg model and the self-consistent Gaussian approximation (SCGA) method⁴⁷. Specifically, the magnetic exchange parameter (J) of Heisenberg model was derived from the DFT calculated total energies of ferromagnetic and G-type antiferromagnetic phases^{48,49}, as shown in Supplementary Fig. S17,

$$J = (E_{\text{AFM}} - E_{\text{FM}}) / (N_{\text{nn}} \cdot N_{\text{mag}}), \quad (1)$$

where E_{AFM} (E_{FM}) is the total energy of the ferromagnetic and antiferromagnetic phases, $N_{\text{mag}} = 4$ is the number of magnetic Ru ions in the unit cell, and $N_{\text{nn}} = 6$ is the number of nearest-neighbour Ru ions of each Ru ion. The Curie temperature was estimated using SCGA method⁴⁷ as

$$T_C^{\text{SCGA}} \approx \frac{1}{3} \theta_C N_{\text{nn}} J, \quad (2)$$

$\theta_C = 0.719$ is a structure dependent parameter⁴⁸.

References

1. Cao, Y. *et al.* Unconventional superconductivity in magic-angle graphene superlattices. *Nature* **556**, 43–50 (2018).
2. Andrei, E. Y. & MacDonald, A. H. Graphene bilayers with a twist. *Nat. Mater.* **19**, 1265–1275 (2020).
3. Pryds, N., Park, D.-S., Jespersen, T. S. & Yun, S. Twisted oxide membranes: A perspective. *APL Mater.* **12**, 010901 (2024).
4. Nuckolls, K. P. & Yazdani, A. A microscopic perspective on moiré materials. *Nat. Rev. Mater.* **9**, 460–480 (2024).
5. Lu, D. *et al.* Synthesis of freestanding single-crystal perovskite films and heterostructures by etching of sacrificial water-soluble layers. *Nat. Mater.* **15**, 1255–1260 (2016).
6. Pesquera, D., Fernández, A., Khestanova, E. & Martin, L. W. Freestanding complex-oxide membranes. *J. Phys.: Condens. Matter* **34**, 383001 (2022).
7. Zhang, J. *et al.* Super-tetragonal Sr₄Al₂O₇ as a sacrificial layer for high-integrity freestanding oxide membranes. *Science* **383**, 388–394 (2024).
8. Sánchez-Santolino, G. *et al.* A 2D ferroelectric vortex pattern in twisted BaTiO₃ freestanding layers. *Nature* **626**, 529–534 (2024).
9. Zubko, P., Catalan, G. & Tagantsev, A. K. Flexoelectric effect in solids. *Annu. Rev. Mater. Res.* **43**, 387–421 (2013).
10. Wang, B., Gu, Y., Zhang, S. & Chen, L.-Q. Flexoelectricity in solids: Progress, challenges, and perspectives. *Prog. Mater. Sci.* **106**, 100570 (2019).
11. Shu, L., Wei, X., Pang, T., Yao, X. & Wang, C. Symmetry of flexoelectric coefficients in crystalline medium. *J. Appl. Phys.* **110**, 104106 (2011).
12. Sha, H. *et al.* Polar vortex hidden in twisted bilayers of paraelectric SrTiO₃. *Nat. Commun.* **15**, 10915 (2024).
13. Haeni, J. H. *et al.* Room-temperature ferroelectricity in strained SrTiO₃. *Nature* **430**, 4 (2004).
14. Yadav, A. K. *et al.* Observation of polar vortices in oxide superlattices. *Nature* **530**, 198–201 (2016).
15. Das, S. *et al.* Observation of room-temperature polar skyrmions. *Nature* **568**, 368–372 (2019).
16. Zabalo, A. & Stengel, M. Switching a polar metal via strain gradients. *Phys. Rev. Lett.* **126**, 127601 (2021).
17. Peng, W. *et al.* Flexoelectric polarizing and control of a ferromagnetic metal. *Nat. Phys.* **20**, 450–455 (2024).
18. Catalan, G. Metal poles around the bend. *Nat. Phys.* **20**, 358–359 (2024).
19. Saeed, U. *et al.* Pervasive protonation of perovskite membranes made by the water-soluble sacrificial layer method. *arXiv:2503.04197* (2025) doi:10.48550/arXiv.2503.04197.
20. Choi, K. J. *et al.* Phase-transition temperatures of strained single-crystal SrRuO₃ thin films. *Adv. Mater.* **22**, 759–762 (2010).
21. Junquera, J. *et al.* Topological phases in polar oxide nanostructures. *Rev. Mod. Phys.* **95**, 025001 (2023).

22. Kornev, I., Fu, H. & Bellaiche, L. Ultrathin films of ferroelectric solid solutions under a residual depolarizing field. *Phys. Rev. Lett.* **93**, 196104 (2004).
23. Meng, M. *et al.* Interface-induced magnetic polar metal phase in complex oxides. *Nat. Commun.* **10**, (2019).
24. Gu, Y. *et al.* Interfacial control of ferromagnetism in ultrathin SrRuO₃ films sandwiched between ferroelectric batio₃ layers. *ACS Appl. Mater. Interfaces* **12**, 6707–6715 (2020).
25. Li, Y. *et al.* Unraveling strain gradient induced electromechanical coupling in twisted double bilayer graphene Moiré superlattices. *Adv. Mater.* **33**, 2105879 (2021).
26. Cai, S. *et al.* Enhanced polarization and abnormal flexural deformation in bent freestanding perovskite oxides. *Nat. Commun.* **13**, 5116 (2022).
27. Lun, Y. *et al.* Ultralow tip-force driven sizable-area domain manipulation through transverse flexoelectricity. *Adv. Mater.* **35**, 2302320 (2023).
28. Allen, P. B. *et al.* Transport properties, thermodynamic properties, and electronic structure of SrRuO₃. *Phys. Rev. B* **53**, 4393–4398 (1996).
29. Eom, C. B. *et al.* Single-crystal epitaxial thin films of the isotropic metallic oxides Sr_{1-x}Ca_xRuO₃ (0 ≤ x ≤ 1). *Science* **258**, 1766–1769 (1992).
30. Gan, Q., Rao, R. A., Eom, C. B., Garrett, J. L. & Lee, M. Direct measurement of strain effects on magnetic and electrical properties of epitaxial SrRuO₃ thin films. *Appl. Phys. Lett.* **72**, 978–980 (1998).
31. Klein, L. *et al.* Transport and magnetization in the badly metallic itinerant ferromagnet. *J. Phys.: Condens. Matter* **8**, 10111–10126 (1996).
32. Hill, N. A. Why are there so few magnetic ferroelectrics? *J. Phys. Chem. B* **104**, 6694–6709 (2000).
33. Spaldin, N. A. & Ramesh, R. Advances in magnetoelectric multiferroics. *Nat. Mater.* **18**, 203–212 (2019).
34. Junquera, J. *et al.* Topological phases in polar oxide nanostructures. *Rev. Mod. Phys.* **95**, 025001 (2023).
35. Han, L. *et al.* High-density switchable skyrmion-like polar nanodomains integrated on silicon. *Nature* **603**, 63–67 (2022).
36. Ngai, J. H., Walker, F. J. & Ahn, C. H. Correlated oxide physics and electronics. *Annu. Rev. Mater. Res.* **44**, 1–17 (2014).
37. Balents, L., Dean, C. R., Efetov, D. K. & Young, A. F. Superconductivity and strong correlations in moiré flat bands. *Nat. Phys.* **16**, 725–733 (2020).
38. Nord, M., Vullum, P. E., MacLaren, I., Tybell, T. & Holmestad, R. Atomap: a new software tool for the automated analysis of atomic resolution images using two-dimensional Gaussian fitting. *Adv. Struct. Chem. Imag.* **3**, 9 (2017).
39. Hýtch, M. J., Snoeck, E. & Kilaas, R. Quantitative measurement of displacement and strain fields from HREM micrographs. *Ultramicroscopy* **74**, 131–146 (1998).
40. Kresse, G. & Furthmüller, J. Efficient iterative schemes for ab initio total-energy calculations using a plane-wave basis set. *Phys. Rev. B* **54**, 11169–11186 (1996).
41. Kresse, G. & Furthmüller, J. Efficiency of ab-initio total energy calculations for metals and semiconductors using a plane-wave basis set. *Comput. Mater. Sci.* **6**, 15–50 (1996).

42. Blöchl, P. E. Projector augmented-wave method. *Phys. Rev. B* **50**, 17953–17979 (1994).
43. Perdew, J. P., Burke, K. & Ernzerhof, M. Perdew, Burke, and Ernzerhof Reply. *Phys. Rev. Lett.* **80**, 891–891 (1998).
44. Perdew, J. P., Burke, K. & Ernzerhof, M. Generalized gradient approximation made simple. *Phys. Rev. Lett.* **77**, 3865–3868 (1996).
45. Lee, S., De Sousa, D. J. P., Jalan, B. & Low, T. Moiré polar vortex, flat bands, and Lieb lattice in twisted bilayer BaTiO₃. *Sci. Adv.* **10**, eadq0293 (2024).
46. Grimme, S., Antony, J., Ehrlich, S. & Krieg, H. A consistent and accurate *ab initio* parametrization of density functional dispersion correction (DFT-D) for the 94 elements H–Pu. *J. Chem. Phys.* **132**, 154104 (2010).
47. Garanin, D. A. Self-consistent Gaussian approximation for classical spin systems: Thermodynamics. *Phys. Rev. B* **53**, 11593–11605 (1996).
48. Huang, A., Hung, S.-H. & Jeng, H.-T. Strain induced metal–insulator transition of magnetic SrRuO₃ single layer in SrRuO₃/SrTiO₃ superlattice. *Appl. Sci.* **8**, 2151 (2018).
49. Jiao, P., Liu, Y., Wang, X. & Chen, J. First principles investigation of Na doping effects on the structural, magnetic, and electronic properties in SrRuO₃. *Comput. Mater. Sci.* **69**, 284–288 (2013).

Acknowledgments

The authors acknowledge support by the National Key Projects for Research and Development of China (Grant No. 2021YFA1400300), the National Natural Science Foundation of China (Grant Nos. 12172047, 12402183, 12374080), the Beijing Natural Science Foundation (Grant No. 1244057). We also acknowledge ICN2 and ALBA (JEMCA) for providing key facilities and technical guidance. ICN2 is supported by the Severo Ochoa program from Spanish MCIN / AEI (Grant No. CEX2021-001214-S), the European Regional Development Fund from European Union (Grant No. IU16-014206 (METCAM-FIB)), and the CERCA Programme, Generalitat de Catalunya. ICN2 is a founding member of e-DREAM. J.A. and X.H. acknowledge funding from Generalitat de Catalunya (Grant No. 2021SGR00457). This study is part of the Advanced Materials programme and was supported by MCIN with funding from European Union NextGenerationEU (PRTR-C17.11) and by Generalitat de Catalunya (In-CAEM Project). We acknowledge support from CSIC Interdisciplinary Thematic Platform (PTI+) on Quantum Technologies (PTI-QTEP+). This work has been funded by the European Commission – NextGenerationEU (Regulation EU 2020/2094), through CSIC's Quantum Technologies Platform (QTEP). Y.L. acknowledges support from the Severo Ochoa Seed Funding program (Grant CEX2021-001214-S/MICIU/AEI/10.13039/501100011033). D.P. acknowledges the “Consolidación Investigadora” grant CNS2024-154522 and grant PID2022-140589NB-I00, funded by MCIN/AEI/10.13039/501100011033. This work is in the framework of the Universitat Autònoma de Barcelona Materials Science PhD program. X.H. acknowledges PhD scholarship support from the China Scholarship Council (CSC) (Grant No. 202304910019). Q.R. acknowledges support from the BIT Research and Innovation Promoting Project Graduate (Grant No. 2023YCXZ002). U.S. acknowledges the funding for this project by Grant PID2019-108573GB-C21 (FOx-Me) funded by the Spanish Ministry of Science and Innovation (DOI: 10.13039/501100011033). I.P.-H. acknowledges funding from AGAUR-FI scholarship (Grant No. 2023FI-00268) Joan Oró of the Secretariat of Universities of the Generalitat of Catalonia and the European SocialPlus Fund. Calculations were performed using resources of the Supercomputer Centre in Chongqing. The authors acknowledge the use of the Spectra 300 microscope, provided under ALBA Synchrotron proposal (Grant No. 20240320035). The authors gratefully acknowledge the assistance of Francesco Salutari, Athique Ahmed Ali and Francisco Javier Belarre Triviño in the preparation of cross-sectional FIB samples, and Bernat Bozzo in the magnetic measurements.

Note: after writing this manuscript, we have become aware of another work on SrRuO₃ membranes (Alejandro Martín Merodio et al., group of Jacobo Santamaría at the Universidad Complutense de Madrid, presented at QUOROM, 22/05/25). So far, they only report transport properties, but we expect their membranes will also display vortices.

Author contributions

Experimental measurements were mainly performed at ICN2 and ALBA (JEMCA), and theoretical calculations were carried out at BIT. All institutions contributed substantially to the development and completion of this work. G.C., J.H., and J.A. designed and

supervised the project. Y.L. conceived the original idea for this work. Y.L. fabricated the thin films and transferred the samples with the help from U.S. and J.M.C.R.. X.H., J.A., B.M., K.G., and I.P. conducted STEM, SAED and TEM experiments. X.H. and Y.L. performed data analysis on the polar vortices, strain gradients, and flexoelectric fields. Q.R., G.T., and J.H. carried out the atomistic simulations and analysis. Y.L. conducted the ferromagnetism and resistance measurements under the guidance of D.P. and X.W.. Y.L. performed the surface morphology measurements. J.P. and J.S. conducted the XRD measurements. Y.M. and Q.L. provided assistance with the experiments. Y.L., X.H. and G.C. wrote the manuscript with the help from all authors. All authors contributed to the discussion of the results and the revision of the manuscript.

Competing interests

The authors declare that they have no competing interests.

Data and materials availability

All data are available in the manuscript or the supplementary information.

Supplementary Information

This PDF file includes:

Supplementary Text I

Supplementary Figures S1 to S17

References

Supplementary Text I: Strain-gradient origin of polar vortices in t-BL SROs

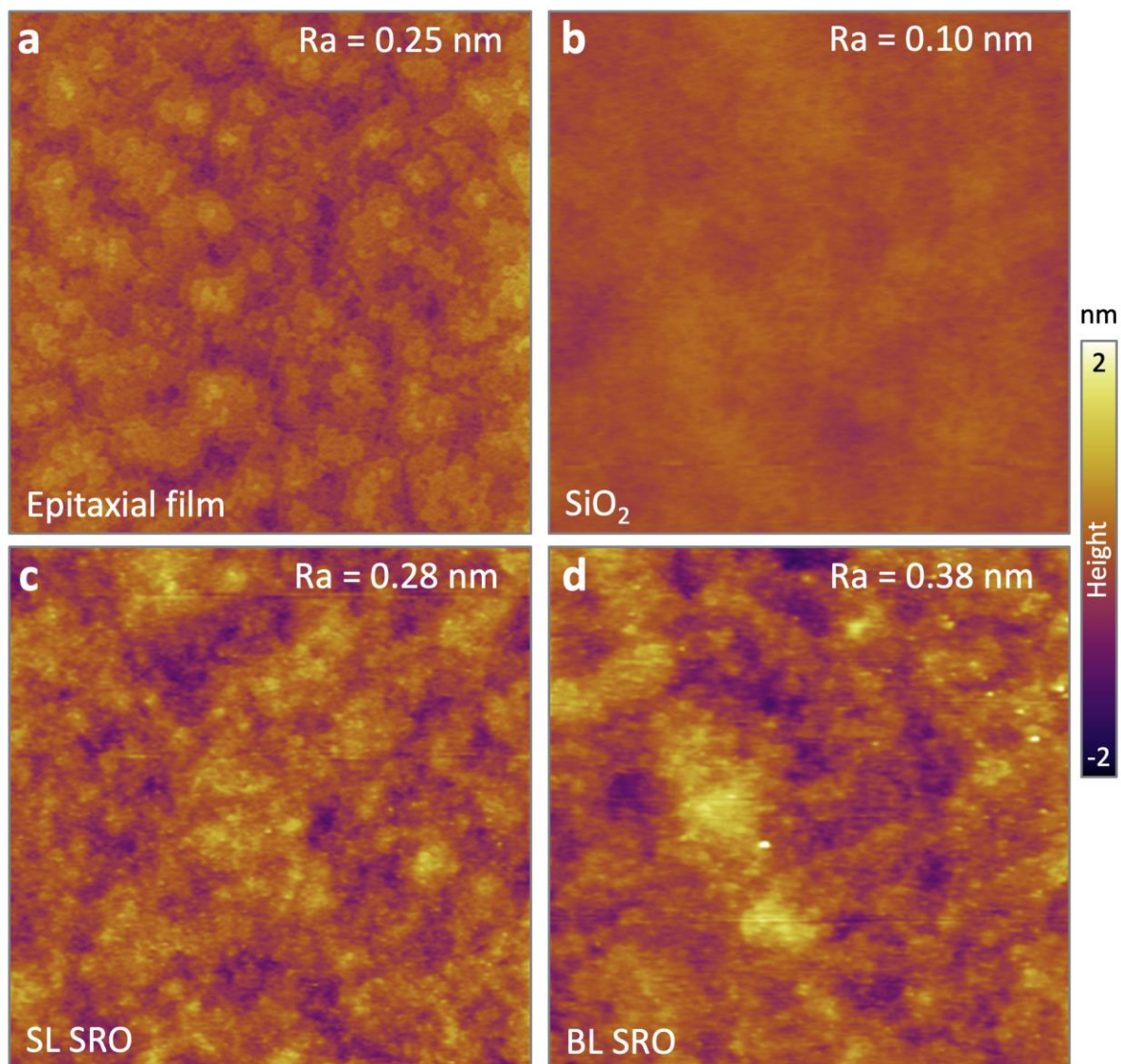
The periodic misalignment of the atoms in the top and bottom layers can generate inhomogeneous interlayer interactions and torsional deformation (shear strain) within the lattice. In principle, the shear strain gradients arisen from inhomogeneous torsion gives rise to flexoelectric fields, which can serve as pseudo-electric fields, modulating polarization and driving the formation of polar vortices. It is nevertheless legitimate to question whether (or how) the flexoelectric effect can still effectively manipulate topological polarization in the presence of electric screening from free charge carriers in a metal. To investigate flexoelectric coupling in metallic SRO bilayers, we employed geometric phase analysis (GPA)¹ to calculate the shear and normal strains (Supplementary Figs. S10 and S11) on the lattice structure observed at STEM-HAADF images (Supplementary Fig. S6). We found that only the shear strains exhibit a periodic distribution that closely follows the moiré pattern and highly correlates with the arrangement of polarization vortices (Fig. 2 in main text). We then computed the derivatives of the shear strain (ε_{xy}) along the x -axis and y -axis to extract the shear strain gradient components ($\varepsilon_{xy,x}$ and $\varepsilon_{xy,y}$) (Supplementary Fig. S10). The corresponding flexoelectric field² can be calculated as

$$\mathbf{E}_{\text{flexo}} = (E_x, E_y) = f_{xyxy}^{\text{eff}} (\varepsilon_{xy,y} \mathbf{E}_i + \varepsilon_{xy,x} \mathbf{E}_j) \quad (\text{S1})$$

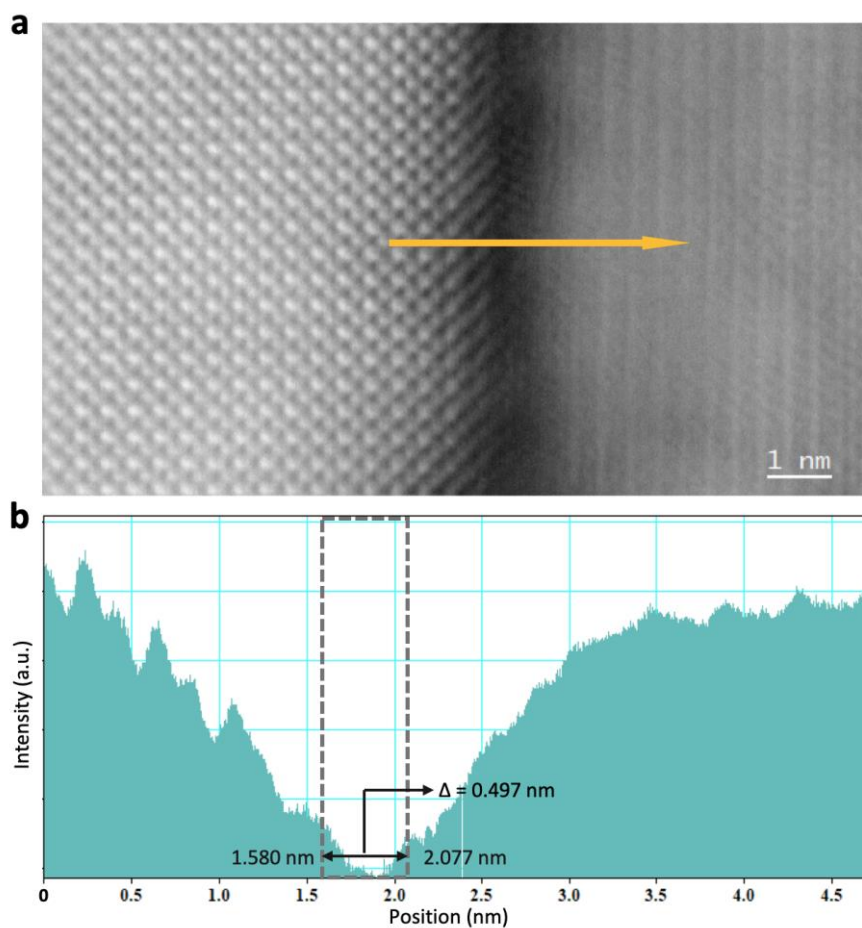
where $\mathbf{E}_{\text{flexo}}$ is a total flexoelectric field. E_x and E_y are in-plane components. \mathbf{E}_i and \mathbf{E}_j are unit vectors in the x -direction and y -direction, respectively. f_{xyxy}^{eff} is an effective flexoelectric coupling coefficient. According to the above model, the shear strain gradients of $\varepsilon_{xy,x}$ and $\varepsilon_{xy,y}$ can generate pseudo-electric field components in the y -direction and x -direction, respectively, which in principle can polarize the lattice both vertically and horizontally. To explore the coupling between strain gradient and polarization, we superimposed the strain gradient maps and the measured Ru displacement components (Supplementary Fig. S10). We find that the strain gradients are distributed in a strip network of alternating signs, with the polarization components pointing in the same direction within each strip region, thus evidencing a direct correlation between the polarization and the direction of the strain gradients. The polarization systematically switches towards the opposite direction upon the reversal of the strain gradients.

On this basis, we reconstructed the total flexoelectric field from the shear strain gradients using eq. (S1) with a unit flexoelectric coefficient. The normalized flexoelectric field maps are presented in Main text Figs. 2j-l and Supplementary Fig. S8, superimposed with the toroidal moment (calculated in a similar way to $Q(\delta_{\text{Ru}})$). The results show a significant correlation between the flexoelectric fields and measured polarization vortices, providing evidence of a flexoelectric (strain gradient) origin for the polar vortices in metallic twisted bilayers. The above-established electromechanical coupling provides further insights into the origin of the observed twist angle-dependent polarization. We compared the shear strains and corresponding strain gradients within different t-BL SROs, and found that they follow the same twist-dependence as polarization (Supplementary Fig. S12). The larger polarization at small angle originates from the more

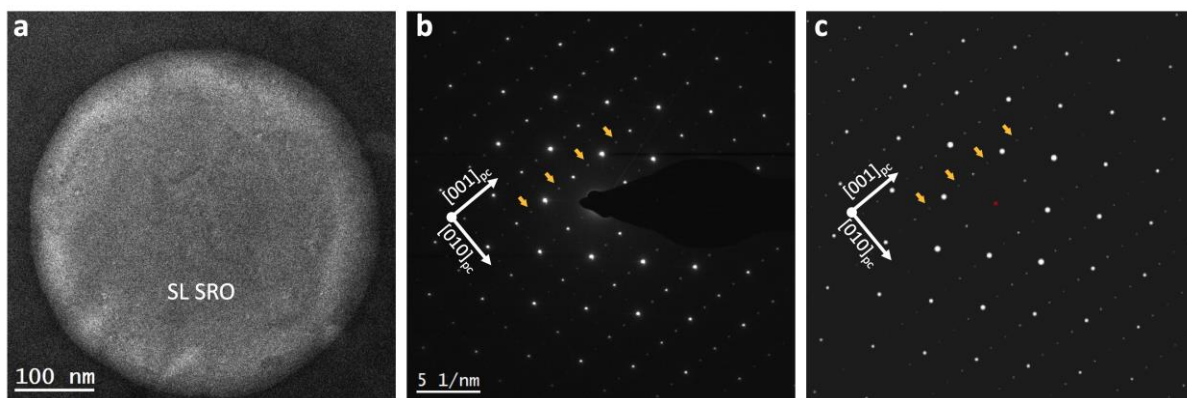
significant lattice distortion (shear strain) and its localized inhomogeneity (strain gradient).



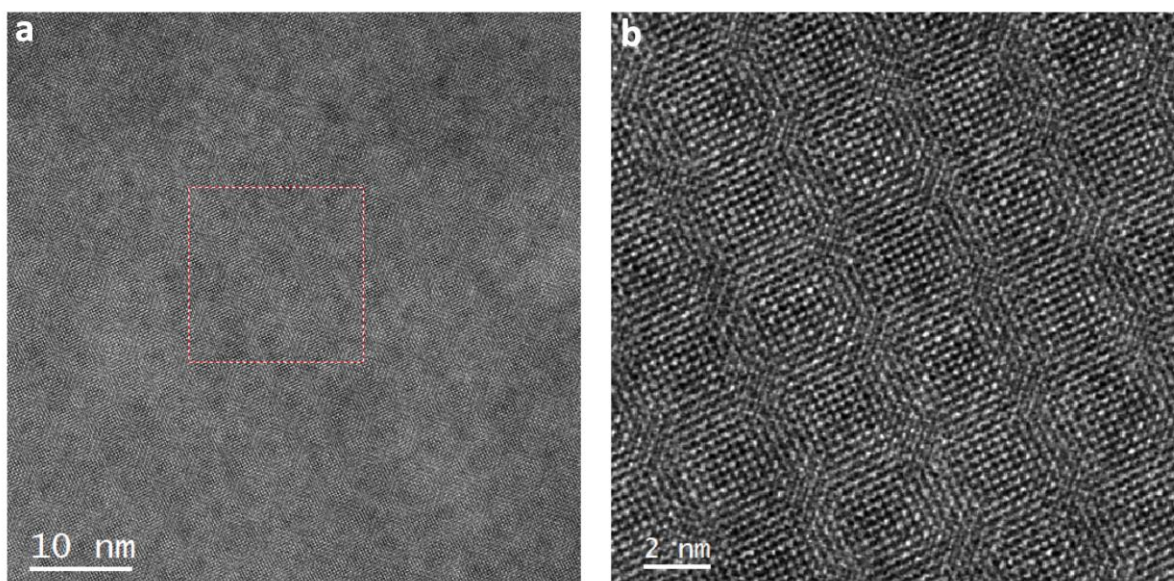
Supplementary Figure S1. High-resolution topographic atomic force microscopy (AFM) images ($2 \times 2 \mu\text{m}^2$) and corresponding surface roughness (Ra) of **a**, epitaxial film, **b**, oxidized silicon substrate, **c**, transferred single layer SRO, and **d**, twisted bilayer SRO.



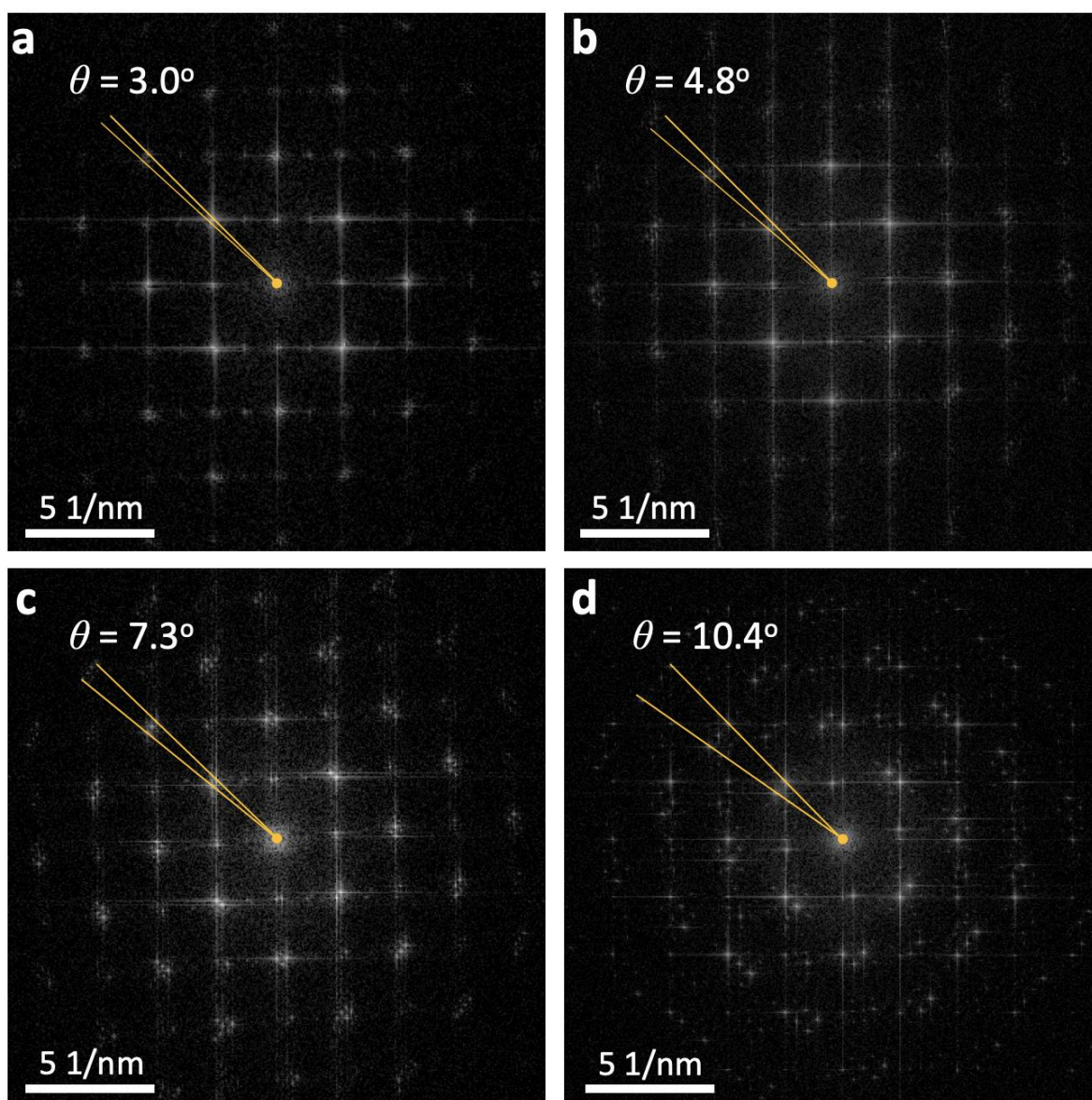
Supplementary Figure S2. **a**, Fourier-filtered STEM-HAADF (cross-section) image of a transferred 4.8° twisted bilayer. **b**, Intensity profile along the highlighted arrow in **a** depicting an interlayer distance of 4.97 Å, which is approximately one unit cell in magnitude.



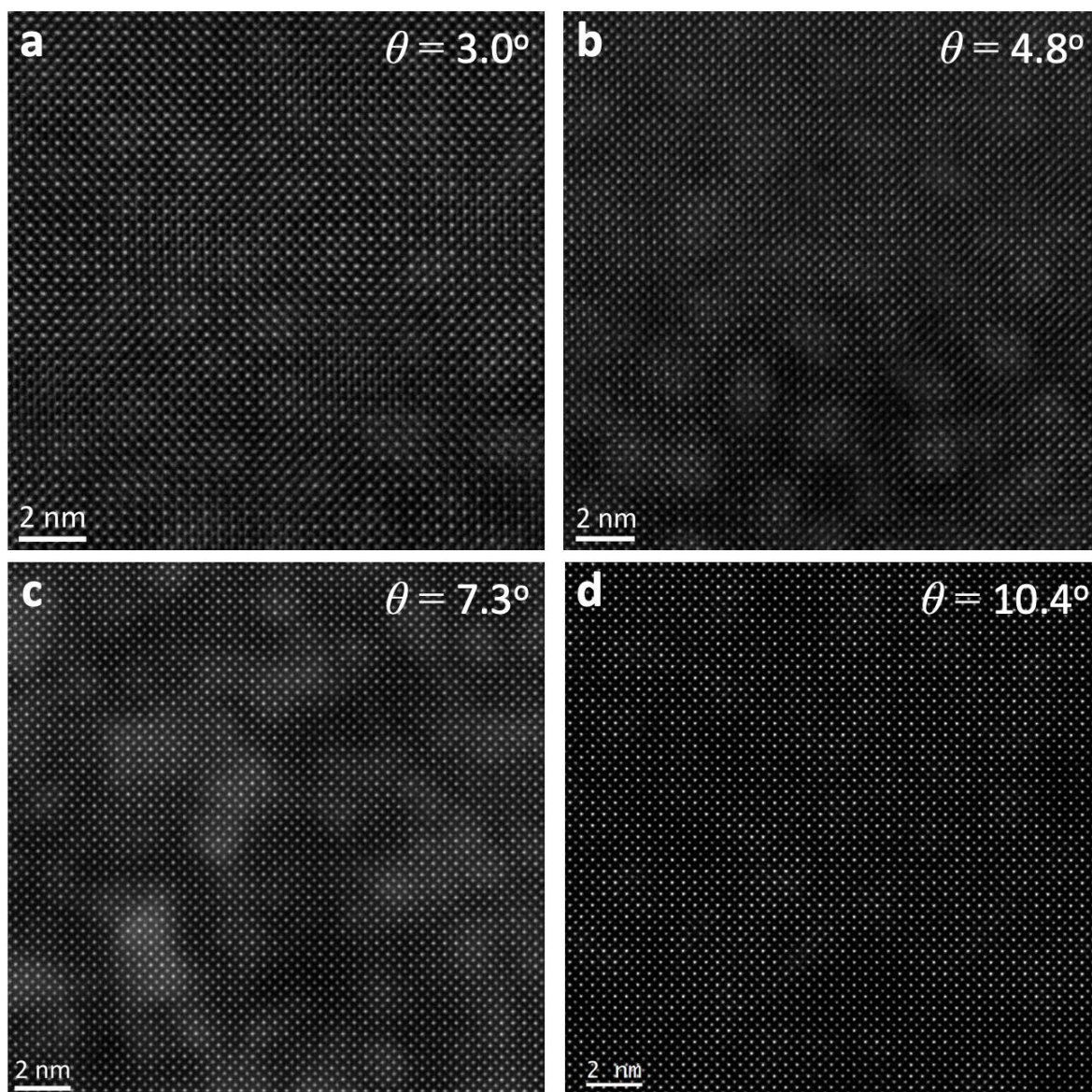
Supplementary Figure S3. **a**, Low-magnification HRTEM image of a freestanding single-layer SRO membrane. **b**, Corresponding selected area electron diffraction (SAED) image. **c**, Simulated SAED pattern of a $[100]_{pc}$ -oriented orthorhombic SRO structure using Recipro software³. The yellow arrows indicate the $\frac{1}{2}$ superlattice diffraction spots. The experimental pattern matches well with the simulated one, indicating orthorhombic characteristics of the freestanding SRO membrane.



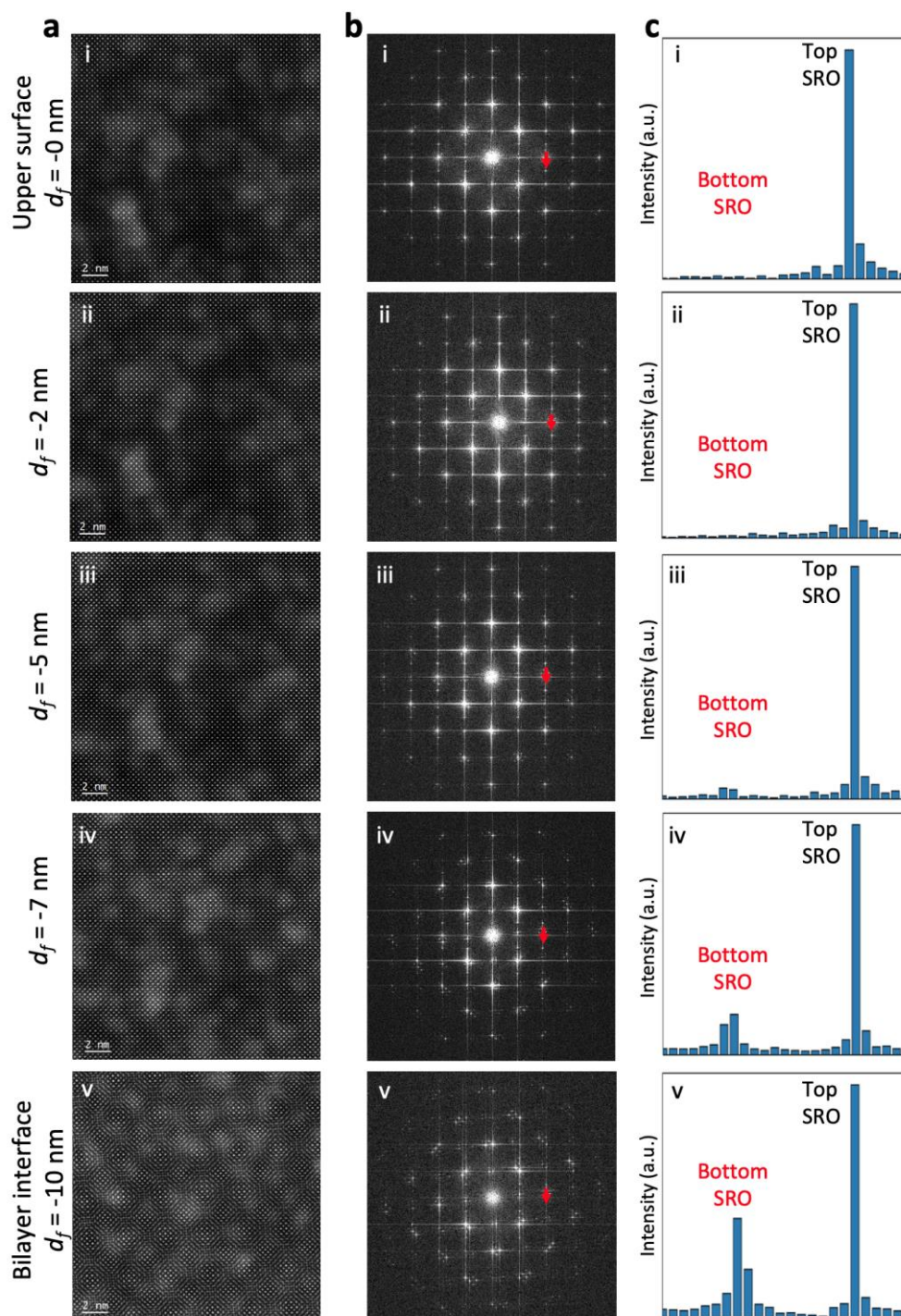
Supplementary Figure S4. **a**, Low-magnification annular dark-field (ADF) image focusing on the bilayer interface of 4.8° twisted bilayer, revealing a continuous and well-ordered moiré pattern. **b**, Magnified view of the region highlighted in **a**, showing detailed moiré features.



Supplementary Figure. S5. a-d, Fast Fourier transform (FFT) patterns corresponding to the STEM-HAADF images focusing on the bilayer interface in the 3.0° , 4.8° , 7.3° , and 10.4° twisted bilayers, respectively. Each FFT pattern exhibits two distinct sets of diffraction spots arising from the top and bottom lattices. The twist angle is determined based on the relative rotation (indicated by two yellow lines) between the two sets of diffraction spots.

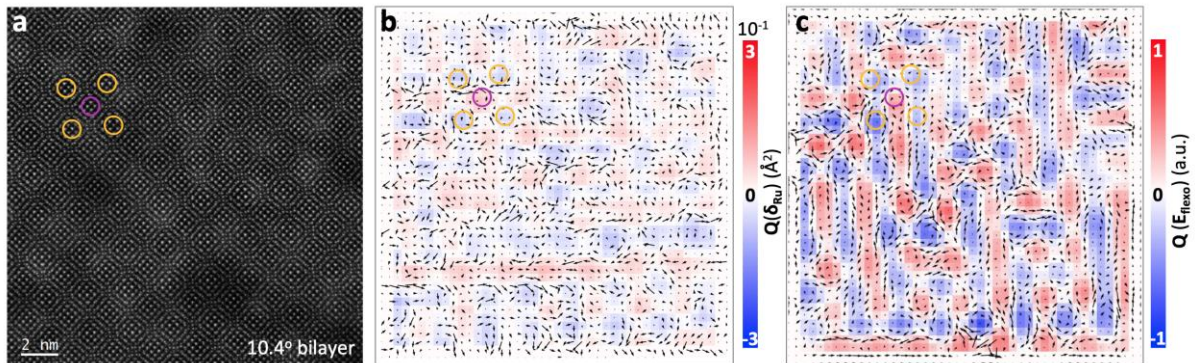


Supplementary Figure. S6. a-d, Planar-view STEM-HAADF images focusing on the upper surface of the top layer in the 3.0° , 4.8° , 7.3° , and 10.4° twisted bilayers, respectively.

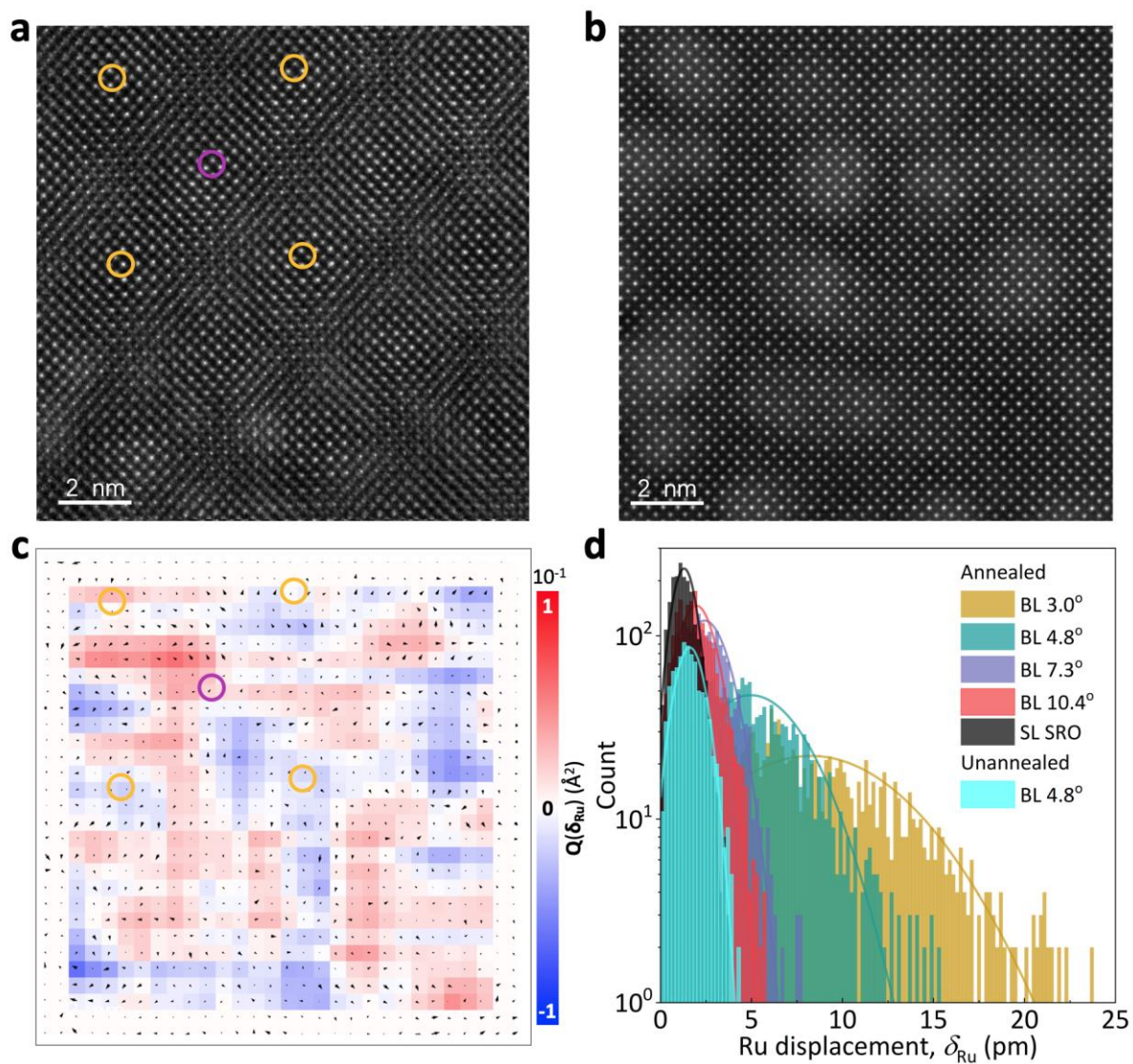


Supplementary Figure S7. **a**, Planar-view STEM-HAADF images of the 7.3° twisted bilayer obtained at different focus depths (d_f), capturing structural variations from the bilayer interface to the upper surface of the top layer. **b**, Corresponding fast Fourier transform (FFT) patterns extracted from the STEM-HAADF images. **c**, Line profiles taken at the $[2-20]_0$ diffraction spots (indicated by red arrows) in the FFT patterns, illustrating the evolution of intensity from the bilayer interface to the upper surface. As shown in Fig. c, the intensity of diffraction spot arisen from bottom SRO layer vanishes gradually as shifting the focus away from bilayer interface to upper surface, indicating that the STEM-

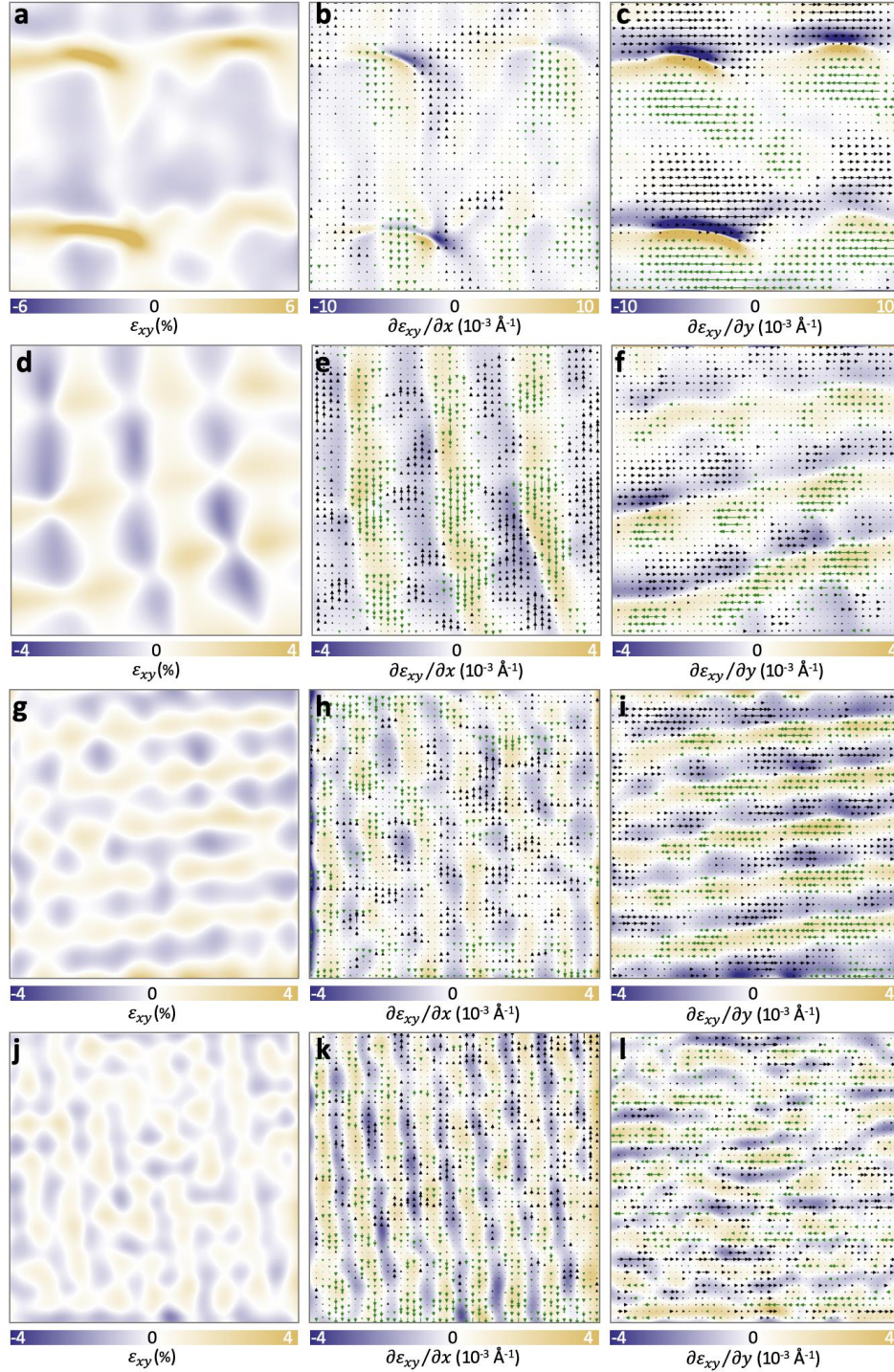
HAADF image focusing on the upper surface selectively captures the lattice structure of the top layer.



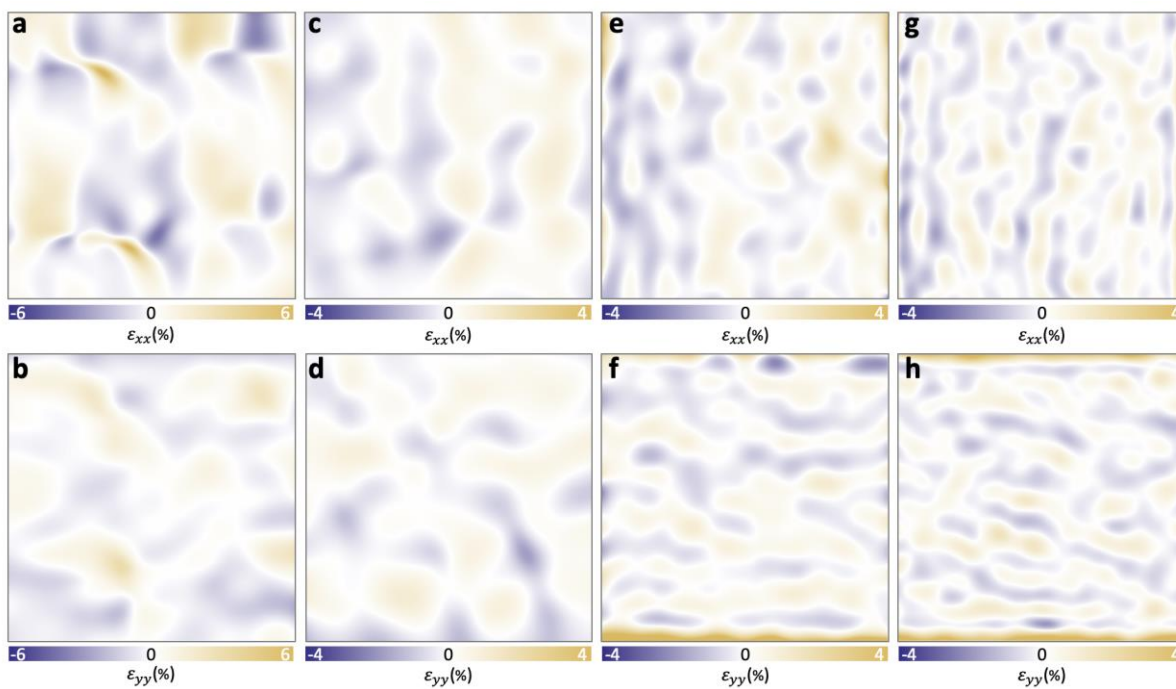
Supplementary Figure. S8. **a**, Planar-view STEM-HAADF images focusing on the interface in the 10.4° twisted bilayer, showing distinct moiré patterns. **b**, Ru displacement maps of the top layer superimposed with their toroidal moment $Q(\delta_{Ru})$. The Ru displacements are amplified by a factor of 120 for clarity. **c**, Normalized flexoelectric field vector maps induced by shear strain gradients in the top layer, superimposed with their toroidal moment $Q(E_{flexo})$. The yellow and purple circles indicate the AA- and AB-stacked regions, respectively.



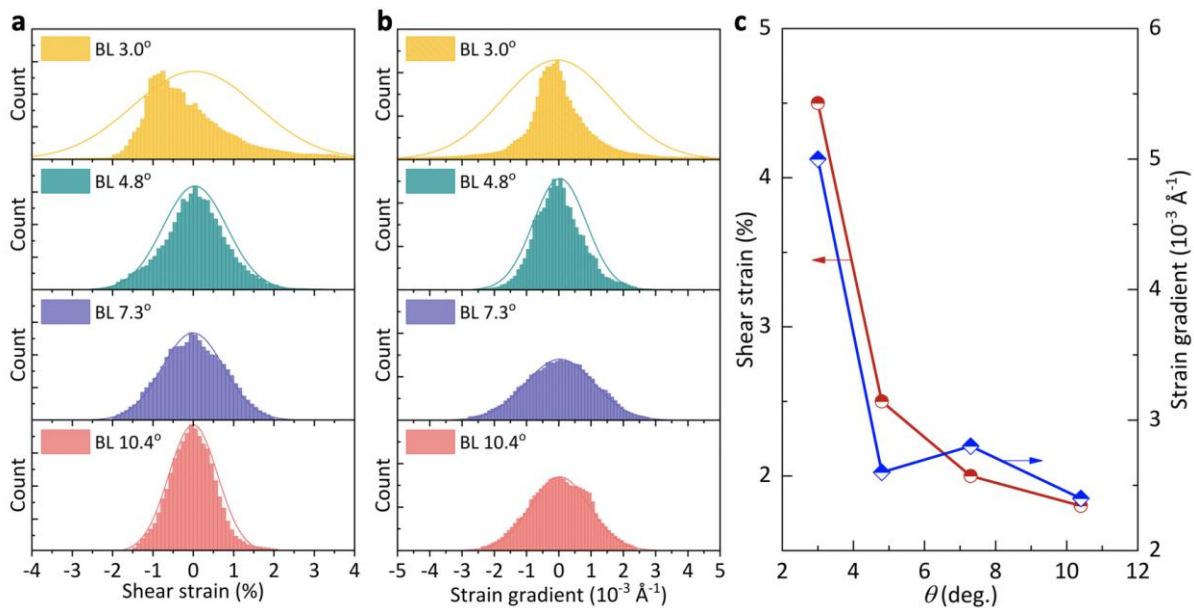
Supplementary Figure. S9. Planar-view STEM-HAADF images of the 4.8° twisted bilayer without annealing, focusing on **a**, the bilayer interface and **b**, the upper surface of the top layer, respectively. **c**, Ru displacement map of the top layer superimposed with the toroidal moment (Q). All Ru displacements are amplified by a factor of 50 (same factor used for the annealed 4.8° twisted bilayer). The yellow and purple circles in **a** and **c** indicate the AA- and AB-stackings. **d**, Histograms comparing the magnitude of Ru displacement in annealed and unannealed samples. As shown in **c** and **d**, the Ru displacements in the unannealed samples are both random and minimal (1.6 pm on average), suggesting a nonpolarized state similar to that of SL SRO.



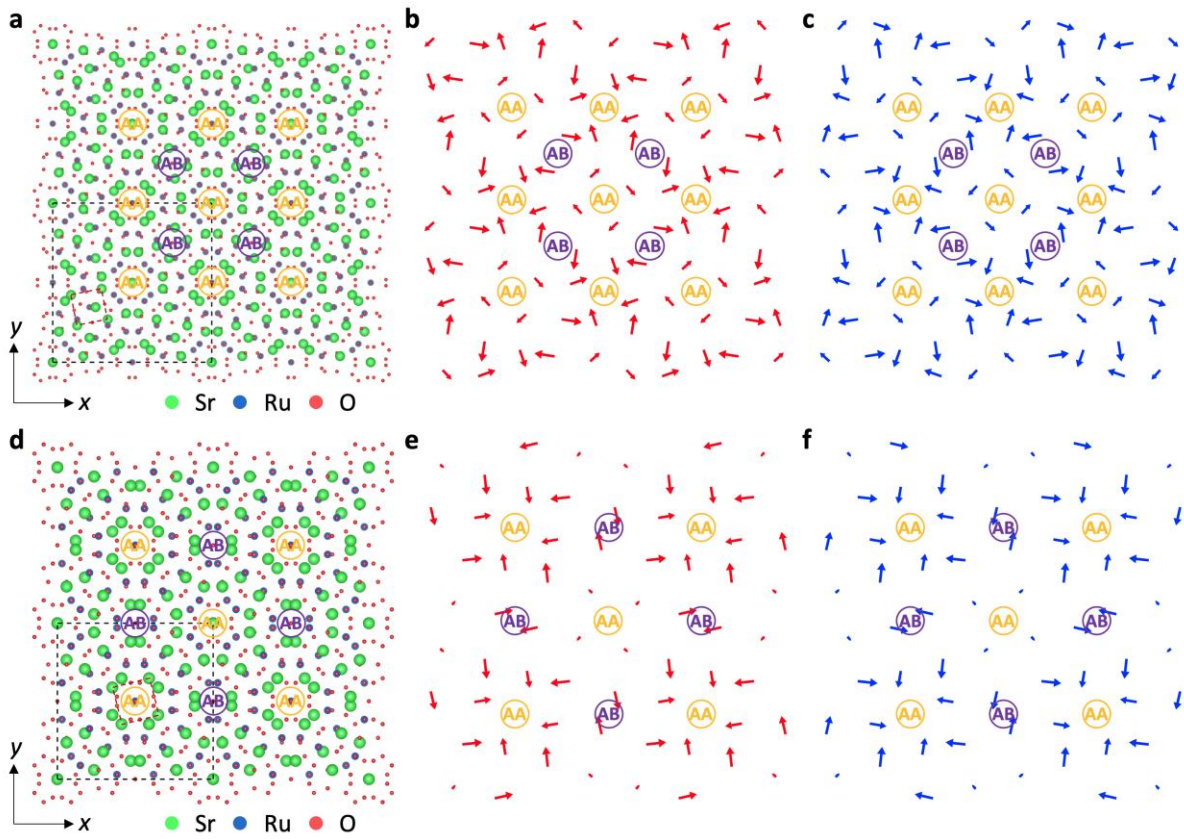
Supplementary Figure. S10. **a**, Shear strain (ϵ_{xy}) component map for the top layer in 3.0° twisted bilayer. **b-c**, Corresponding shear strain gradient maps along the x-axis and y-axis, respectively, superimposed with Ru displacement components along the y-axis and x-axis. The strain gradients ($\epsilon_{xy,x}$ and $\epsilon_{xy,y}$) can generate flexoelectric field components in the y-direction and x-direction, respectively. Same shear strain (gradients) analyses for **d-f**, the 4.8° twisted, **g-i**, the 7.4° twisted and **j-l**, the 10.4° twisted bilayers. The Ru displacement components in **b-c**, **e-f**, **g-i**, and **j-l** are amplified by a factor of 30, 50, 100, and 120 for clarity, respectively.



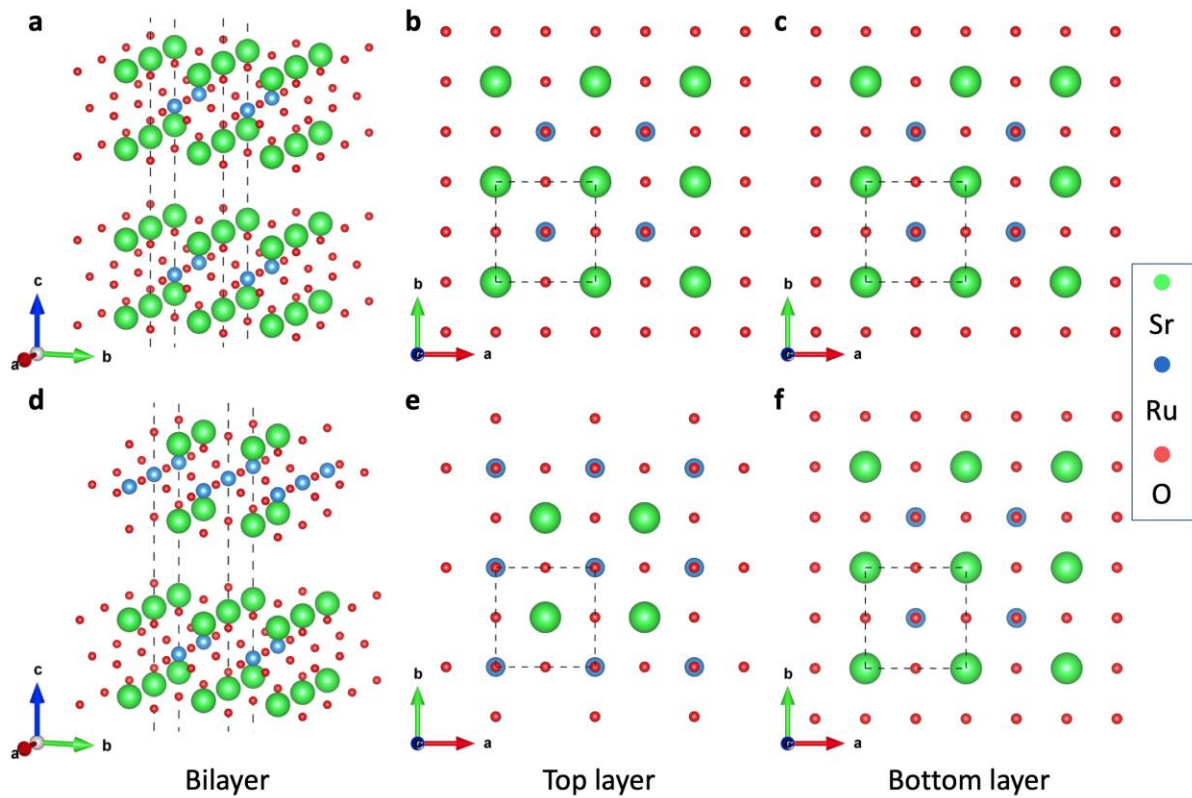
Supplementary Figure S11. **a**, Normal strain (ϵ_{xx}) along the x -axis and **b**, normal strain (ϵ_{yy}) along the y -axis of the top layer in the 3.0° twisted bilayer. Same strain analyses for **c-d**, the 4.8° twisted, **e-f**, the 7.3° twisted, and **g-h**, the 10.4° twisted bilayers.



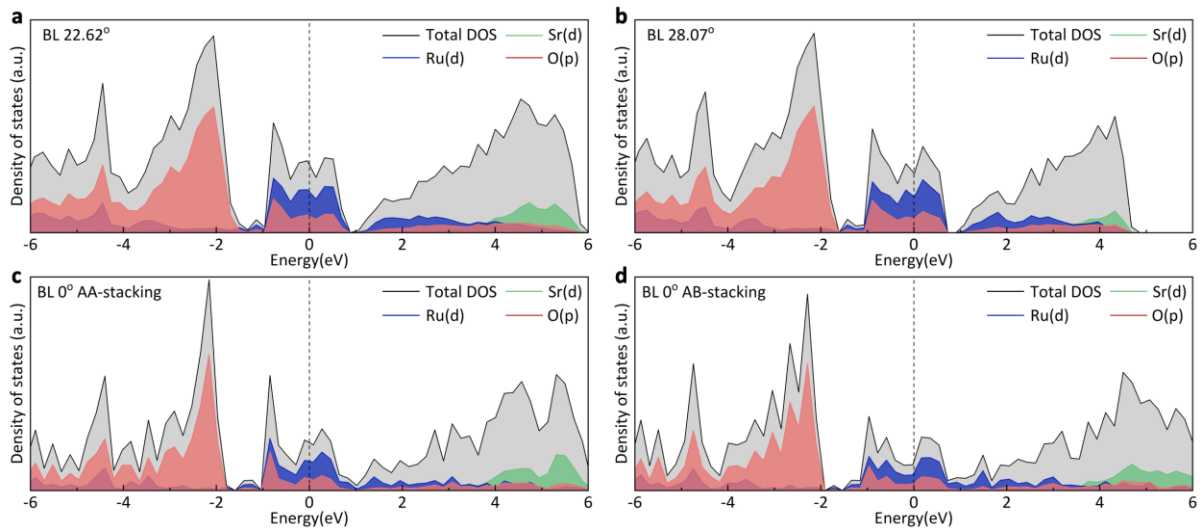
Supplementary Figure S12. Histograms comparing **a**, the shear strains and **b**, shear strain gradients of t-BL SROs. **c**, Twist angle dependence of the maximum absolute strain and strain gradient.



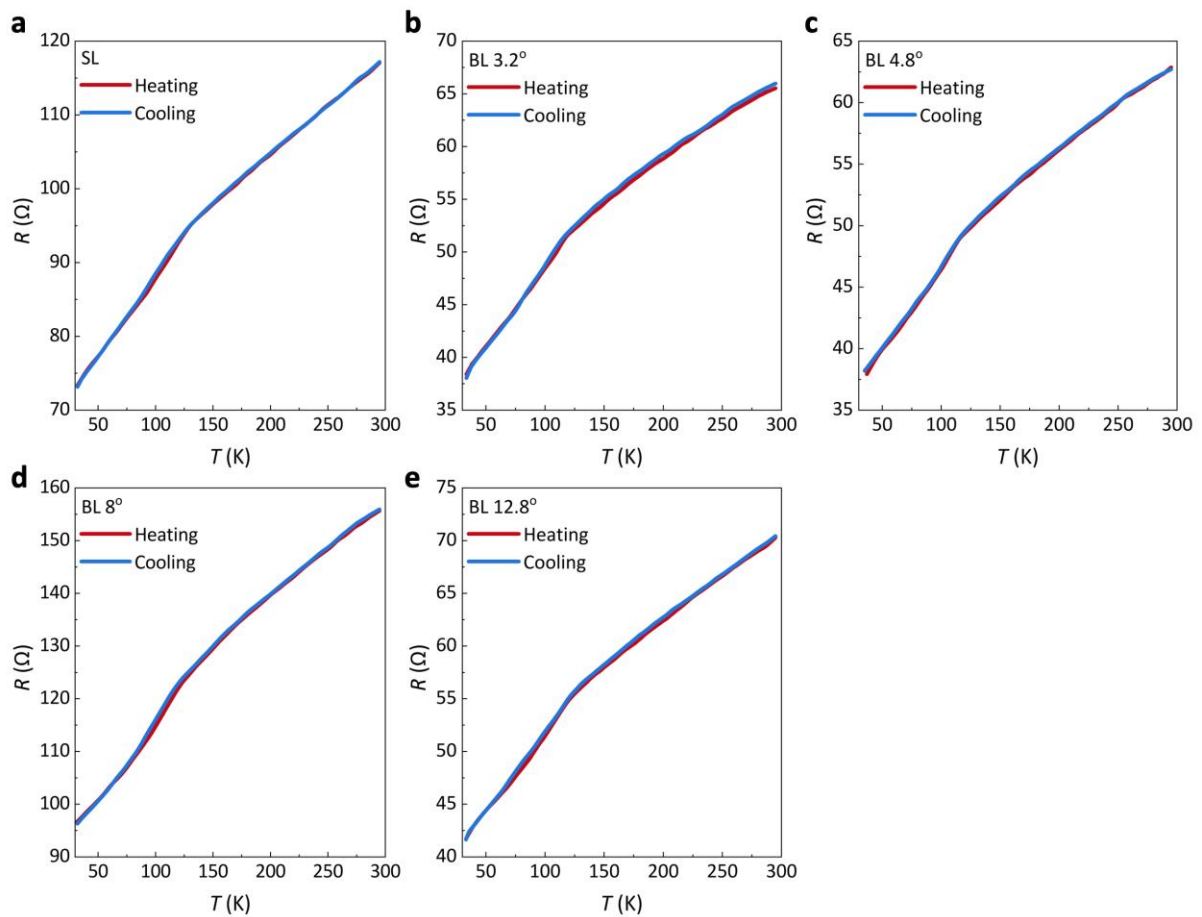
Supplementary Figure S13. **a**, Planar-view of constructed 2x2 supercell for the 22.62° twisted bilayer. The black and red dashed squares denote the supercell and unit cell, respectively. **b-c**, In-plane Ru displacement maps of the top and bottom SRO layers, respectively. **d-f**, Same analyses for the 28.07° twisted bilayer. All displacements are amplified by a factor of 25 for clarity. The AA- and AB-stacked regions are marked with yellow and purple circles, respectively.



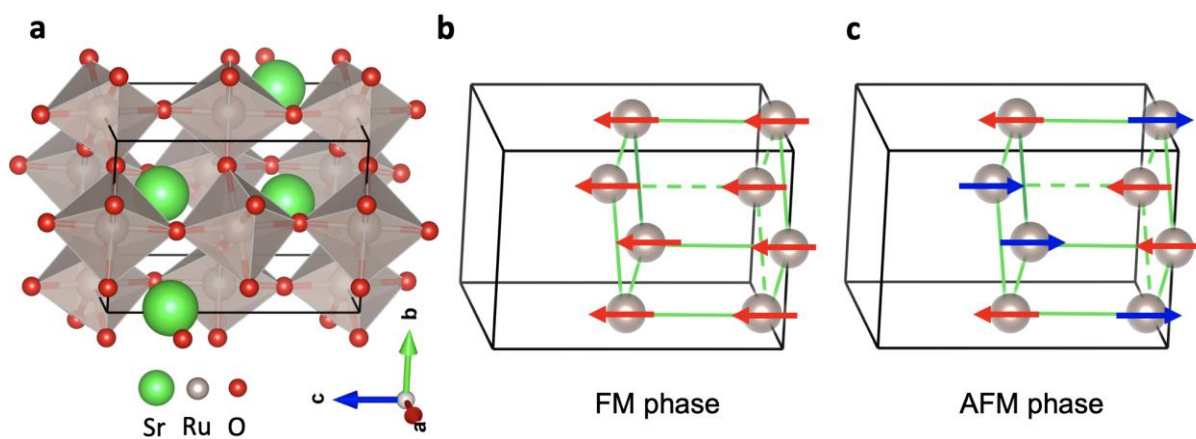
Supplementary Figure S14. **a**, 3D-view of the constructed 2x2 supercell structure for the 0° -stacked bilayer with AA-stacking. **b-c**, Planar-view of the relaxed lattice of the top layer and bottom layer, respectively. **d-f**, Same calculations for 0° -stacked bilayer with AB-stacking. Irrespective of AA- or AB-stacked configurations, the SRO maintains a centrosymmetric structure without any Ru displacement.



Supplementary Figure S15. Electronic density of states (DOS) of **a**, the polarized 22.62° twisted bilayer. **b-d**, Same calculations for the polarized 28.07° twisted bilayer, and the unpolarized 0° -stacked bilayer with AA- and AB-stackings, respectively. All results show nonzero density of states at the Fermi level, primarily contributed by the *d*-orbital electrons of Ru atoms, suggesting that SRO retains its metallic nature in both twisted and un-twisted bilayers.



Supplementary Figure S16. Temperature-dependent resistance curves of SL and BL SROs with twist angles ranging from 3.2° to 12.8°. The measurements were conducted separately in heating and cooling modes under a temperature range of 35 - 295 K. The heating and cooling curves coincide with each other. Accurately comparing the resistance among t-BL SROs is challenging due to the difficulty in precisely determining the conductive area, which is affected by unavoidable microcracks.



Supplementary Figure S17. **a**, Orthorhombic structure of SrRuO₃ used in DFT magnetic calculation. Spin configurations of **b**, ferromagnetic (FM) and **c**, G-type antiferromagnetic (AFM) phase.

References

1. Hýtch, M. J., Snoeck, E. & Kilaas, R. Quantitative measurement of displacement and strain fields from HREM micrographs. *Ultramicroscopy* **74**, 131–146 (1998).
2. Ma, W. A study of flexoelectric coupling associated internal electric field and stress in thin film ferroelectrics. *Phys. Stat. Sol. (b)* **245**, 761–768 (2008).
3. Seto, Y. & Ohtsuka, M. ReciPro: free and open-source multipurpose crystallographic software integrating a crystal model database and viewer, diffraction and microscopy simulators, and diffraction data analysis tools. *J. Appl. Crystallogr.* **55**, 397–410 (2022).